

Precursors of fatty alcohols in the ISM: Discovery of *n*-propanol

Izaskun Jiménez-Serra¹, Lucas F. Rodríguez-Almeida¹, Jesús Martín-Pintado¹, Víctor M. Rivilla^{1,2}, Mattia Melosso³, Shaoshan Zeng⁴, Laura Colzi^{1,2}, Yoshiyuki Kawashima⁵, Eizi Hirota⁶, Cristina Puzzarini³, Belén Tercero⁷, Pablo de Vicente⁷, Fernando Rico-Villas¹, Miguel A. Requena-Torres^{8,9} and Sergio Martín^{10,11}

¹ Centro de Astrobiología (CSIC/INTA), Ctra. de Torrejón a Ajalvir km 4, E-28806, Torrejón de Ardoz, Spain
e-mail: ijimenez@cab.inta-csic.es

² INAF-Osservatorio Astrofisico di Arcetri, Largo Enrico Fermi 5, 50125, Florence, Italy

³ Dipartimento di Chimica "Giacomo Ciamician", Università di Bologna, via F. Selmi 2, 40126, Bologna, Italy

⁴ Star and Planet Formation Laboratory, Cluster for Pioneering Research, RIKEN, 2-1 Hirosawa, Wako, Saitama, 351-0198, Japan

⁵ Department of Applied Chemistry, Faculty of Engineering, Kanagawa Institute of Technology, Atsugi, Kanagawa 240-0292, Japan

⁶ The Graduate University for Advanced Studies, Hayama, Kanagawa 240-0193, Japan

⁷ Observatorio de Yebes (IGN), Cerro de la Palera s/n, E-19141, Guadalajara, Spain

⁸ University of Maryland, College Park, ND 20742-2421, USA

⁹ Department of Physics, Astronomy and Geosciences, Towson University, MD 21252, USA

¹⁰ European Southern Observatory, Alonso de Córdova 3107, Vitacura 763 0355, Santiago, Chile

¹¹ Joint ALMA Observatory, Alonso de Córdova 3107, Vitacura 763 0355, Santiago, Chile

Received September 15, 1996; accepted March 16, 1997

ABSTRACT

Context. Theories on the origins of life propose that early cell membranes were synthesized from amphiphilic molecules simpler than phospholipids such as fatty alcohols. The discovery in the interstellar medium (ISM) of ethanolamine, the simplest phospholipid head group, raises the question whether simple amphiphilic molecules are also synthesized in space.

Aims. We investigate whether precursors of fatty alcohols are present in the ISM.

Methods. For this, we have carried out a spectral survey at 7, 3, 2 and 1 mm toward the Giant Molecular Cloud G+0.693-0.027 located in the Galactic Center using the IRAM 30 m and Yebes 40 m telescopes.

Results. Here, we report the detection in the ISM of the primary alcohol *n*-propanol (in both conformers *Ga*-*n*-C₃H₇OH and *Aa*-*n*-C₃H₇OH), a precursor of fatty alcohols. The derived column densities of *n*-propanol are $(5.5 \pm 0.4) \times 10^{13} \text{ cm}^{-2}$ for the *Ga* conformer and $(3.4 \pm 0.3) \times 10^{13} \text{ cm}^{-2}$ for the *Aa* conformer, which imply molecular abundances of $(4.1 \pm 0.3) \times 10^{-10}$ for *Ga*-*n*-C₃H₇OH and of $(2.5 \pm 0.2) \times 10^{-10}$ for *Aa*-*n*-C₃H₇OH. We also searched for the *AGa* conformer of *n*-butanol [*AGa*-*n*-C₄H₉OH] without success yielding an upper limit to its abundance of $\leq 4.1 \times 10^{-11}$. The inferred CH₃OH:C₂H₅OH:C₃H₇OH:C₄H₉OH abundance ratios go as 1:0.04:0.006:≤0.0004 toward G+0.693-0.027, i.e. they decrease roughly by one order of magnitude for increasing complexity. We also report the detection of both *syn* and *anti* conformers of vinyl alcohol, with column densities of $(1.11 \pm 0.08) \times 10^{14} \text{ cm}^{-2}$ and $(1.3 \pm 0.4) \times 10^{13} \text{ cm}^{-2}$, and abundances of $(8.2 \pm 0.6) \times 10^{-10}$ and $(9.6 \pm 3.0) \times 10^{-11}$, respectively.

Conclusions. The detection of *n*-propanol, together with the recent discovery of ethanolamine in the ISM, opens the possibility that precursors of lipids according to theories of the origin of life, could have been brought to Earth from outer space.

Key words. ISM: molecules – ISM: clouds – Galaxy: centre – astrochemistry – line: identification

1. Introduction

Compartmentalization (i.e. the formation of vesicles or small membranes) is an essential step in the emergence of life. Theories of the origin of life such as prebiotic systems chemistry (Ruiz-Mirazo et al. 2014), propose that compartmentalization had to appear concurrently with the first metabolic and replicative systems forming proto-cells. It is believed that the composition of primordial membranes was much simpler than that of modern cells. Several families of amphiphilic molecules such as alkyl phosphates, alkyl sulfates, fatty acids, and fatty alcohols have been proposed as possible prebiotic lipids, i.e. as constituents of proto-membranes (Ruiz-Mirazo et al. 2014). Among them, fatty alcohols (also called primary alcohols) present a simple structure consisting of a straight-chain with the OH group linked to a primary carbon (i.e. forming a -CH₂OH group).

Two possible scenarios have been proposed for the formation of prebiotic lipids: they could form *endogenously* under early

Earth conditions via e.g. Fischer-Tropsch synthesis (Nooner et al. 1976; McCollom et al. 1999; Ruiz-Mirazo et al. 2014); or they could be synthesised *exogenously* in interstellar space and incorporated to Solar-system materials such as interplanetary dust particles, comets and meteorites (Bernstein et al. 1999). Although not all examined meteorites contain long-chain amphiphiles (Deamer et al. 1994), Deamer (1985) showed that the amphiphilic compounds found in the Murchison meteorite can form vesicle-like structures under certain prebiotic conditions. Using the different contributions to organic matter delivery analysed by Chyba & Sagan (1992, see their Table 2), Ruiz-Mirazo et al. (2014) estimated that a total amount of $\sim 10^{16}$ - 10^{18} kg of extraterrestrial organic matter was delivered to Earth during the Late Heavy Bombardment period (mainly between 3.9 and 3.8 billions of years ago), which supports the idea that extraterres-

trial material could have contributed to the emergence of prebiotic lipids in an early Earth¹.

The recent discovery of ethanolamine (NH₂CH₂CH₂OH), the simplest head group of phospholipids (Rivilla et al. 2021a), in the interstellar medium (ISM), has raised the interest for the search of precursors of prebiotic lipids in space, and in particular of other alcohols. For fatty alcohols, the only ones that have been observed in the ISM are methanol (CH₃OH) and ethanol (C₂H₅OH), which are practically ubiquitous in the ISM (see e.g. Jorgensen et al. 2020; Martín et al. 2021, and references therein). *n*-propanol (also named 1-propanol; molecular formula CH₃CH₂CH₂OH or C₃H₇OH) has been searched for in the ISM, but no detection has been reported to date (Tercero et al. 2015; Müller et al. 2016; Qasim et al. 2019; Manigand et al. 2021). However, primary alcohols, including propanol, have been detected in comet 67P/Churyumov-Gerasimenko (Altwegg et al. 2019), which suggests that this molecule could be formed under interstellar conditions.

In this work, we report the discovery of *n*-propanol toward the Giant Molecular Cloud (GMC) G+0.693-0.027 (hereafter G+0.693) located in the Galactic Center. We also report the detection of both *syn* and *anti* conformers of vinyl alcohol (CH₂CHOH) toward the same cloud. The *syn* conformer was tentatively detected toward SgrB2(N) by Turner & Aponi (2001), but this detection was never confirmed in higher-sensitivity observations carried out with ALMA (Martin-Drumel et al. 2019). More recently, Agúndez et al. (2021) have unambiguously identified the *syn* conformer toward TMC-1. However, to our knowledge this is the first time that the *anti* conformer of this molecule is robustly detected in the ISM.

G+0.693 is known to be one of the most chemically-rich interstellar sources in our Galaxy (Requena-Torres et al. 2006, 2008; Zeng et al. 2018), despite the fact it does not show any sign of high-mass star-formation activity (Zeng et al. 2020). The chemistry of this cloud is characterized by the presence of low-velocity shocks (its emission shows broad linewidths of ~ 20 km s⁻¹ and high abundances of HNC, a typical molecular tracer of low-velocity shocks; Martín et al. 2008), which sputter the molecular content of the icy mantles of dust grains into the gas phase (see e.g. Jiménez-Serra et al. 2008). The H₂ gas densities in G+0.693 are of the order of a few 10⁴ cm⁻³ (Zeng et al. 2020) and the gas kinetic temperatures range from 70 to 150 K, as measured using CH₃CN (Zeng et al. 2018). Due to the low H₂ gas densities, the molecular line emission from high dipole moment molecules such as complex organics is sub-thermally excited, and their excitation temperature lies below 20 K (Requena-Torres et al. 2006; Zeng et al. 2018). This represents an advantage for the search of new molecular species since the millimeter spectra observed toward this source present rather low levels of line blending and line confusion. As a result, G+0.693 has yielded several first detections of new molecular species in the ISM including Z-cyanomethanimine (Z-HNCHCN; Rivilla et al. 2019), hydroxylamine (NH₂OH; Rivilla et al. 2020), ethanolamine (NH₂CH₂CH₂OH; Rivilla et al. 2021a), cyanomethyl radical (HNCN; Rivilla et al. 2021b), mono-thioformic acid (HC(O)SH; Rodríguez-Almeida et al. 2021a), ethyl isocyanate (C₂H₅NCO; Rodríguez-Almeida et al. 2021b) and PO⁺ (Rivilla et al. 2022). Urea, an important prebiotic molecule (Becker et al. 2019; Belloche et al. 2019), has also been detected toward this cloud (Jiménez-Serra et al. 2020).

The paper is organised as follows. In Section 2, we describe the observations, and in Section 3 we present the detections of *n*-propanol and the *syn* and *anti* forms of vinyl alcohol. We also report the upper limits to the non-detections of isopropanol (i-C₃H₇OH), ethyl methyl ether (CH₃OCH₂CH₃), cyclopropanol (c-C₃H₅OH) and *n*-butanol (n-C₄H₉OH). In Section 4, we discuss the chemistry of *n*-propanol and vinyl alcohol and put these detections in context with previous works and with theories for the origin of life. Finally, in Section 5 we present our conclusions.

2. Observations

We have carried out a spectral line survey at 1 mm, 2 mm, 3 mm and 7 mm toward G+0.693 with the Instituto de Radioastronomía Milimétrica (IRAM) 30 m telescope (Granada, Spain) and the Yebes 40m telescope (Guadalajara, Spain). The spectral coverage goes from 32 GHz to 233 GHz and the data were smoothed to a typical velocity resolution of ~ 1.5 - 2.5 km s⁻¹. The equatorial coordinates of the source are α (J2000)= $17^{\text{h}}47^{\text{m}}22^{\text{s}}$ and δ (J2000)= $-28^{\circ}21'27''$. We used the position switching mode with an off position located at ($-885''$, $290''$) with respect to G+0.693. Each frequency setup was repeated shifting the central frequency by 20-100 MHz in order to identify spurious lines or contamination from the image band.

The IRAM 30m observations were performed during three sessions in 2019: 10-16th of April, 13-19th of August and 11-15th of December. The EMIR E090, E150, and E230 receivers were used together with the fast Fourier transform spectrometers (FFTS) with a frequency resolution of 200 kHz (equivalent to a velocity resolution between 0.8 km s⁻¹ and 0.26 km s⁻¹ at 3 mm and 1 mm, respectively). The IRAM 30m beam size ranged from $\sim 34''$ to $11''$ when going from 72 to 233 GHz. The observations with the Yebes 40m radiotelescope were carried out between the 3rd-9th and 15th-22nd of February 2020. The Nanocosmos Q-band (7 mm) HEMT receiver was used which enabled ultra broad-band observations with an instantaneous bandwidth of 18.5 GHz per polarization between 31.3 GHz and 50.6 GHz (Tercero et al. 2021). The 16 FFTS provided a channel width of 38 kHz, which corresponds to a velocity resolution of 0.22-0.36 km s⁻¹. The Yebes 40m beam size ranged from $\sim 54''$ to $36''$ when moving from 31 to 50 GHz. The line intensity of all spectra was measured in units of T_A* as the molecular emission toward G+0.693 is extended compared to the main beam of the telescopes (Requena-Torres et al. 2006; Zeng et al. 2020).

3. Analysis and results

3.1. Detection of the *Ga* and *Aa* conformers of *n*-propanol

We have used the data analysis package MADCUBA² (Martín et al. 2019) to search for all transitions from the *Ga*, *Aa*, *Gg*, and *Gg'* conformers of *n*-propanol (or 1-propanol) within our dataset (see Figure 1). We could not search for the *Ag* conformer because its energy levels are heavily perturbed by the *Aa* species and the spectroscopic parameters have never been reported (see Kisiel et al. 2010). The relative energies of the *n*-propanol conformers are: E=0 K for *Ga*, E=40.3 K for *Aa*, E=64.7 K for *Ag*, E=68.8 K for *Gg*, and E=73.2 K for *Gg'* (Kisiel et al. 2010).

¹ Note that the total amount of organic matter in the present biosphere is about 6×10^{14} kg (Bar-On et al. 2018).

² MADCUBA, or MADrid Data CUBe Analysis, is a software developed at the Center of Astrobiology in Madrid: <https://cab.inta-csic.es/madcuba/index.html>

Table 1. Unblended or slightly blended transitions of *Ga-n*-C₃H₇OH and *Aa-n*-C₃H₇OH detected towards G+0.693.

Frequency (MHz)	QNs ($J''_{K_a, K_c} - J''_{K_a', K_c'}$)	E _u (K)	log I(300K) (nm ² MHz)	rms (mK)	δv (km s ⁻¹)	$\int T_A^* dv$ (mK km s ⁻¹)	S/N ^a	blending
<i>Ga-n</i>-C₃H₇OH								
40341.1539	3 _{1,2} -2 _{0,2}	3.3	-6.4573	1.1	1.9	28.9(6.5) ^b	4.5	blended with C ₂ H ₅ NCO
88449.6240	7 _{1,6} -6 _{0,6}	13.6	-5.6188	1.1	4.2	47.5(9.9)	4.8	clean transition
94895.9659	5 _{3,2} -4 _{2,2}	11.0	-5.5443	3.2	1.9	63.2(20.0)	3.2	blended with HCCCC ¹³ CN
97219.5786	11 _{0,11} -10 _{1,10}	28.8	-5.0046	2.4	3.8	63.6(20.8)	3.1	clean transition
105032.7600*	4 _{4,1} -3 _{3,0}	11.9	-5.3260	2.2	1.7	335.6(13.0) ^c	25.7 ^c	clean transition ^{c,d}
105032.8215*	4 _{4,0} -3 _{3,0}	11.9	-5.3814	2.2	1.7	-	-	-
105034.6719*	4 _{4,1} -3 _{3,1}	11.9	-5.3814	2.2	1.7	-	-	-
105034.7334*	4 _{4,0} -3 _{3,1}	11.9	-5.3259	2.2	1.7	-	-	-
133685.6682*	5 _{5,0} -4 _{4,1}	18.3	-5.0148	4.1	7.3	354.9(50.0) ^c	7.1 ^c	slightly blended with CH ₃ COCH ₃ ^{c,d}
133685.6682*	5 _{5,1} -4 _{4,0}	18.3	-5.0148	4.1	7.3	-	-	-
133685.6682*	5 _{5,1} -4 _{4,1}	18.3	-5.0718	4.1	7.3	-	-	-
133685.6682*	5 _{5,0} -4 _{4,0}	18.3	-5.0718	4.1	7.3	-	-	-
143143.8136*	6 _{5,2} -5 _{4,1}	21.1	-4.9557	1.5	1.7	320.2(8.5) ^c	37.7 ^c	clean transition ^{c,d}
143143.8332*	6 _{5,1} -5 _{4,1}	21.1	-5.0037	1.5	1.7	-	-	-
143144.1096*	6 _{5,1} -5 _{4,2}	21.1	-4.9557	1.5	1.7	-	-	-
143144.1096*	6 _{5,2} -5 _{4,2}	21.1	-5.0037	1.5	1.7	-	-	-
162029.4986*	8 _{5,4} -7 _{4,3}	27.9	-4.8415	2.1	6.0	238.8(22.7) ^c	10.5 ^c	slightly blended with CH ₃ CHO ^{c,d}
162030.2797*	8 _{5,3} -7 _{4,3}	27.9	-4.8688	2.1	6.0	-	-	-
162039.5868*	8 _{5,4} -7 _{4,4}	27.9	-4.8687	2.1	6.0	-	-	-
162040.3663*	8 _{5,3} -7 _{4,4}	27.9	-4.8415	2.1	6.0	-	-	-
162332.1928*	6 _{6,0} -5 _{5,1}	26.1	-4.7688	4.2	6.0	307.0(46.0) ^c	6.7 ^c	slightly blended with HSC ^c
162332.1928*	6 _{6,1} -5 _{5,0}	26.1	-4.7688	4.2	6.0	-	-	-
162332.1928*	6 _{6,1} -5 _{5,1}	26.1	-4.8267	4.2	6.0	-	-	-
162332.1928*	6 _{6,0} -5 _{5,0}	26.1	-4.8267	4.2	6.0	-	-	-
<i>Aa-n</i>-C₃H₇OH								
34110.7596	12 _{1,11} -12 _{0,12}	29.1	-5.4467	0.9	2.2	33.6(6.0) ^b	5.6	clean transition
44022.8732	3 _{1,3} -2 _{0,2}	3.2	-5.8803	2.2	1.7	71.0(12.8)	5.5 ^c	clean transition
73921.2560	9 _{2,8} -9 _{1,9}	20.2	-5.1140	2.8	2.5	69.2(20.0)	3.5	blended with U species
77153.9362*	8 _{1,8} -7 _{0,7}	13.6	-5.0315	1.4	2.4	134.2(9.3)	14.4	slightly blended with n-C ₃ H ₇ CN ^d
83485.2943*	9 _{1,9} -8 _{0,8}	16.7	-4.9139	2.3	2.2	128.9(15.0)	8.6	clean transition ^d
89742.8720*	10 _{1,10} -9 _{0,9}	20.2	-4.8060	1.6	2.0	118.6(10.3)	11.5	slightly blended with (CH ₂ OH) ₂ and U-line ^d
89850.2691*	3 _{2,2} -2 _{1,1}	6.5	-5.3442	1.3	2.0	98.0(8.3)	11.8	clean transition ^d
90618.9845*	3 _{2,1} -2 _{1,2}	6.5	-5.3441	2.4	2.0	97.3(15.3)	6.4	slightly blended with HCC ¹³ CN
150358.3345*	5 _{3,3} -4 _{2,2}	15.1	-4.6853	2.9	1.6	144.2(16.6)	8.7	clean transition
150390.2490*	5 _{3,2} -4 _{2,3}	15.1	-4.6852	2.9	1.6	144.2(16.6)	8.7	clean transition

Notes. ^(a) The S/N ratios are calculated from the integrated intensity of the lines inferred from the LTE fits of MADCUBA-SLIM. Note that they are not calculated from the gaussian fits of individual lines. ^(b) The error in the integrated intensity is calculated as $\text{rms} \times \sqrt{\delta v} \times \Delta v$, with δv the velocity resolution of the spectra and Δv the FWHM of the line emission of 20 km s⁻¹. ^(c) The line corresponds to a blend of four individual *Ga-n*-C₃H₇OH transitions. The total integrated intensity and the S/N ratio are calculated from the sum of the areas of the individual transitions. ^(d) Transitions detected at the ≥ 3 rms noise level in peak intensity. ^(e) This S/N ratio should be taken with caution since the LTE fit carried out by MADCUBA-SLIM overpredicts the integrated intensity of the line. ^(f) Transitions that provide the identification of the species with S/N ≥ 6 in integrated intensity.

We note, however, that the conformers of *n*-propanol were modelled independently (i.e. without taking into account their zero-point energy) as it has been done in the past for other species toward G+0.693 such as imines, for which both the low- and high-energy conformers have been detected (see Rivilla et al. 2019). Our data reveal that only the two lowest energy conformers, *Ga* and *Aa* (hereafter *Ga-n*-C₃H₇OH and *Aa-n*-C₃H₇OH, respectively; see Figure 1), are detected toward G+0.693 (see below). The spectroscopic information of *Ga-n*-C₃H₇OH has been extracted from the Cologne Database for Molecular Spectroscopy catalog (CDMS, entry 060505; Endres et al. 2016), which has been derived from the rotational spectrum measured by Kisiel et al. (2010). The spectroscopic information for the rest of the conformers of *n*-propanol, has been obtained by us using the data from Dreizler & Scappini (1981) and Kisiel et al. (2010).

The line identification and analysis of the transitions of *Ga-n*-C₃H₇OH and *Aa-n*-C₃H₇OH was carried out using the SLIM (Spectral Line Identification and Modelling) tool of MADCUBA. SLIM uses the spectroscopic data entries from the molecular catalogs to generate synthetic spectra under the assumption of Local Thermodynamic Equilibrium (LTE) and by considering line opacity effects. The LTE fit that best matches the observed line spectra of *Ga-n*-C₃H₇OH and *Aa-n*-C₃H₇OH provides the derived values for the molecular column densities

(N), excitation temperatures (T_{ex}), central radial velocities of the gas (v_{LSR}) and full widths at half maximum (FWHM) of the line emission.

Figures 2 and 3 present the unblended and slightly blended transitions of *Ga-n*-C₃H₇OH and *Aa-n*-C₃H₇OH, respectively, detected toward G+0.693. Table 1 reports the spectroscopic information of the transitions from these species together with the rms noise level measured in the spectra (rms), the derived integrated line intensities ($\int T_A^* dv$) and the signal-to-noise (S/N) ratios (also in integrated intensity) obtained with MADCUBA-SLIM. The rms noise level (rms) was calculated at the velocity resolution reported in Table 1 using all the line-free parts of each spectrum within a velocity range of ± 200 km s⁻¹ around each line. For those spectra where not enough line-free parts were available, a velocity range of ± 600 km s⁻¹ around each line was used. To improve the visualization of the detected lines, some of the spectra have been smoothed to a velocity resolution of 4-8 km s⁻¹, enough to provide ≥ 3 resolution elements over the linewidth. We stress that the smoothing of the lines does not affect our analysis in any form as demonstrated by Rivilla et al. (2020).

In Figures 2 and 3 and Table 1, we indicate with asterisks the transitions that provide the identification of *Ga-n*-C₃H₇OH and *Aa-n*-C₃H₇OH. All these transitions have S/N ≥ 6 , where

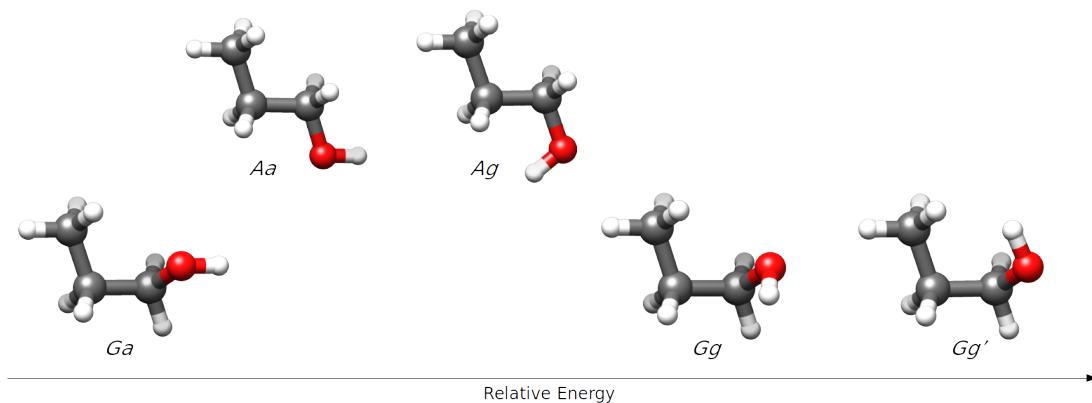


Fig. 1. Conformers of *n*-propanol ($n\text{-C}_3\text{H}_7\text{OH}$) represented as a function of relative energy. The two lowest energy conformers are the *Ga* and *Aa* conformers, which have been detected toward G+0.693 (see Section 3.1). Note that the x-axis is not to scale for visualisation purposes. The relative energies of the different conformers of *n*-propanol are: $E=0$ K for *Ga*, $E=40.3$ K for *Aa*, $E=64.7$ K for *Ag*, $E=68.8$ K for *Gg*, and $E=73.2$ K for *Gg'* (see also Section 3.1).

the error in the integrated intensity of the lines is calculated as $\text{rms} \times \sqrt{\delta v \times \Delta v}$, where δv is the velocity resolution of the spectra and Δv is the FWHM of the line emission. Note, however, that if a more conservative approach were taken (i.e. if we considered Δv as the full velocity range covered by the line), then the S/N ratios would be lower by a factor $\text{sqrt}(2)=1.4$. This would not affect the identification of the species reported here because all the bright lines that contribute to the identification of *Ga-n-C*₃H₇OH and *Aa-n-C*₃H₇OH would have $\text{S/N} \geq 4.5$ even after correcting by this factor. The rest of transitions of *Ga-n-C*₃H₇OH and *Aa-n-C*₃H₇OH reported in Table 1 and Figures 2 and 3 without asterisks, demonstrate that they are consistent with the species identification and their LTE fits. Figures 2 and 3 also show the $3 \times \text{rms}$ noise level in peak intensity (black dotted lines) and the $3 \times \text{rms} / \sqrt{N}$ level (with N the number of channels across the FWHM), which is associated with the noise level in integrated intensity, i.e. our detectability criterion (see red dotted lines).

The $6_{6,X} \rightarrow 5_{5,X}$, $4_{4,X} \rightarrow 3_{3,X}$, and $3_{1,2} \rightarrow 2_{0,2}$ transitions of *Ga-n-C*₃H₇OH at 162332 MHz, 105032 MHz, and 40341 MHz, respectively (see Figure 2), are partly blended with HSC, *s*-propanal and C₂H₅NCO lines of similar intensity (see the detections of some of these species in Rivilla et al. 2020; Rodríguez-Almeida et al. 2021b). However, we note that the global LTE fit (i.e. considering all molecular species) of the spectra at these frequencies, matches perfectly the observed spectra (see black histograms and blue solid lines in Figure 2). For *Aa-n-C*₃H₇OH (see Figure 3), the $10_{1,10} \rightarrow 9_{0,9}$ and $9_{2,8} \rightarrow 9_{1,9}$ transitions are likely blended with lines from unidentified species, besides a small contribution from (CH₂OH)₂ for the $10_{1,10} \rightarrow 9_{0,9}$ line (see Table 1). The derived S/N ratio of the $3_{1,3} \rightarrow 2_{0,2}$ transition should be taken with caution since the LTE fit performed by MADCUBA-SLIM overpredicts the integrated intensity of this line. The rest of *Ga-n-C*₃H₇OH and *Aa-n-C*₃H₇OH transitions considered in our analysis but not shown here, are consistent with their MADCUBA-SLIM LTE fits but appear heavily blended with lines from other molecular species.

The best LTE fit of the *Ga-n-C*₃H₇OH lines is obtained for a column density of $N(\text{Ga-n-C}_3\text{H}_7\text{OH}) = (5.5 \pm 0.4) \times 10^{13} \text{ cm}^{-2}$ and a $T_{\text{ex}} = 14$ K, $V_{\text{LSR}} = 65.9 \pm 1.0 \text{ km s}^{-1}$ and $\Delta v = 20 \text{ km s}^{-1}$ (T_{ex} and Δv needed to be fixed for the SLIM-AUTOFIT algorithm to find convergence). For *Aa-n-C*₃H₇OH, the best fit of the lines was reached for a $N(\text{Aa-n-C}_3\text{H}_7\text{OH}) = (3.4 \pm 0.3) \times 10^{13} \text{ cm}^{-2}$ and

a $T_{\text{ex}} = 12.5 \pm 2.0$ K, after fixing the central radial velocity and the FWHM of the source to $V_{\text{LSR}} = 69 \text{ km s}^{-1}$ and $\Delta v = 20 \text{ km s}^{-1}$. The derived and assumed T_{ex} , V_{LSR} and Δv are consistent with those measured for other molecular species toward this source (see e.g. Requena-Torres et al. 2006; Zeng et al. 2018; Rivilla et al. 2020; Rodríguez-Almeida et al. 2021a; Rivilla et al. 2021a), and with the results obtained from the rotational diagrams of *Ga-n-C*₃H₇OH and *Aa-n-C*₃H₇OH shown in Figures A.1 and A.2 in the Appendix.

To derive the abundances of the *Ga* and *Aa* conformers of propanol, we assume a H₂ column density of $1.35 \times 10^{23} \text{ cm}^{-2}$ as measured toward G+0.693 (Martín et al. 2008). This provides an abundance of $(4.1 \pm 0.3) \times 10^{-10}$ for *Ga-n-C*₃H₇OH and of $(2.5 \pm 0.2) \times 10^{-10}$ for *Aa-n-C*₃H₇OH. The abundance ratio between the two detected conformers of *n*-propanol is $\text{Ga}/\text{Aa} = 1.64$. Considering this ratio and that the *Aa* conformer lies ~ 40 K above *Ga*, one can check whether these two isomers are in thermodynamic equilibrium. By using Equation 3 of Rivilla et al. (2019), the derived T_{kin} is ~ 80 K, consistent with the kinetic temperature range measured from CH₃CN toward G+0.693 (between 70 and 150 K; see Zeng et al. 2018). The calculated Ga/Aa abundance ratio therefore suggests that both species are in thermodynamic equilibrium (understood as the equilibration between the abundances of the *Ga* and *Aa* conformers) as observed for other species such as the E/Z isomers of imines (see García de la Concepción et al. 2021).

The derived upper limits to the other two conformers of *n*-propanol for which spectroscopic data exist (*Gg* and *Gg'*), are presented in Table 2. They have been calculated using the rms noise level of the brightest, less-blended transition spectra, and assuming a $T_{\text{ex}} = 12.5$ K, i.e. the same T_{ex} as the one inferred from *Aa-n-C*₃H₇OH (see above). The derived upper limits to their column densities and abundances are, respectively, $\leq 1.6 \times 10^{13} \text{ cm}^{-2}$ and $\leq 1.2 \times 10^{-10}$ for *Gg-n-C*₃H₇OH, and $\leq 5.7 \times 10^{12} \text{ cm}^{-2}$ and $\leq 4.2 \times 10^{-11}$ for *Gg'-n-C*₃H₇OH (see Table 2).

By using the abundance ratios Ga/Gg and Ga/Gg' , we can investigate whether the *Gg* and *Gg'* conformers are also in thermodynamic equilibrium. The derived abundance ratios $\text{Ga}/\text{Gg} \geq 3.4$ and $\text{Ga}/\text{Gg}' \geq 9.7$ yield kinetic temperatures $T_{\text{kin}} \leq 56$ K and $T_{\text{kin}} \leq 32$ K, respectively. These kinetic temperatures are lower than the ones measured toward G+0.693 (Zeng et al. 2018), which suggests that only the lower energy conformers of a molecular species could reach thermodynamic equilibrium via mechanisms such as multi-dimensional quantum tunneling as

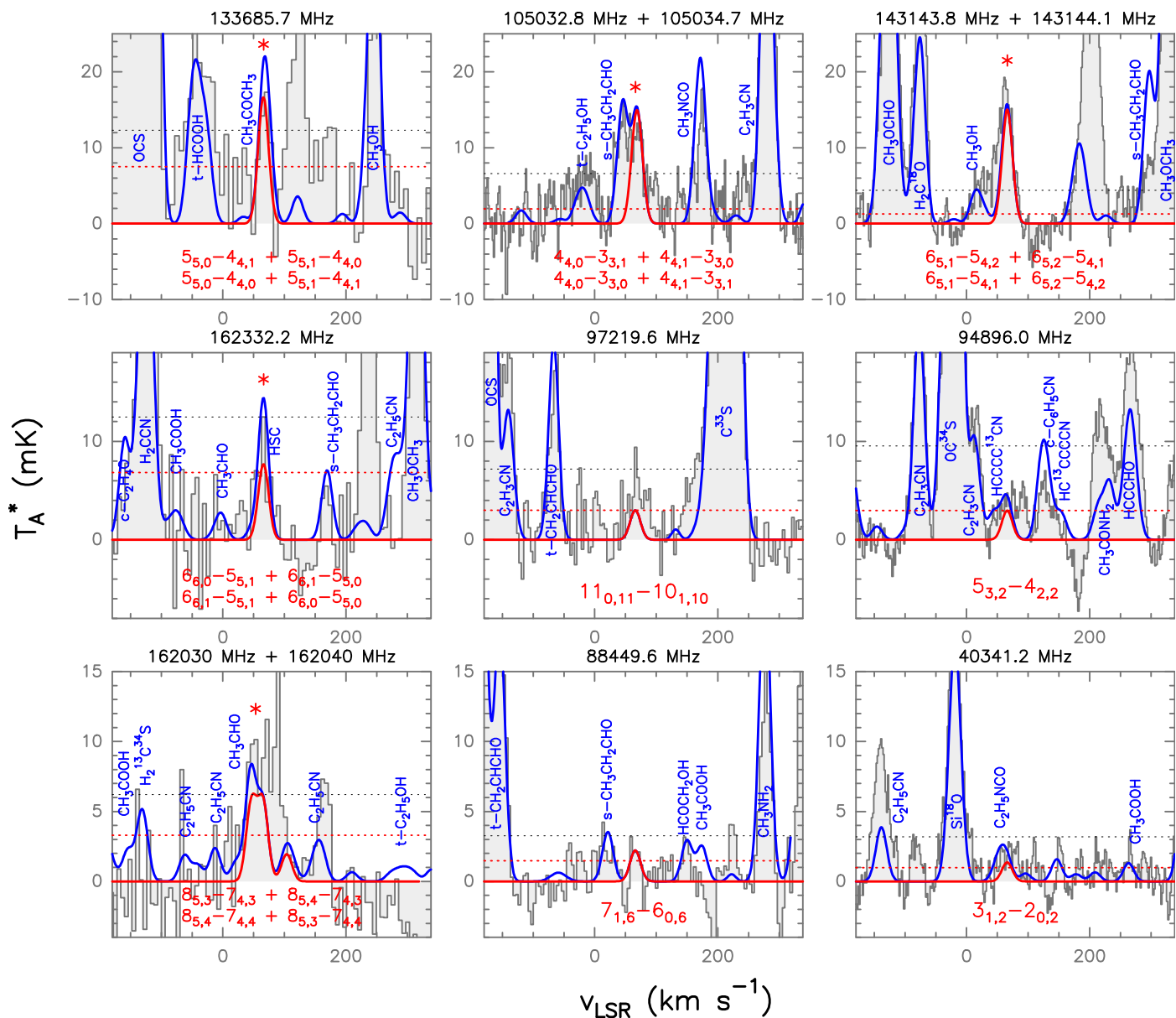


Fig. 2. Unblended and slightly blended transitions of *Ga-n*-C₃H₇OH detected toward G+0.693. Histogram and grey shaded area correspond to the observed IRAM 30m and Yebes 40m spectra. Red lines indicate the best LTE fit to the lines of *Ga-n*-C₃H₇OH reported in Table 1. Blue lines show the overall fit to the observed spectra considering all molecular species detected in G+0.693. The quantum numbers of the *Ga-n*-C₃H₇OH transitions are indicated in red at the bottom part of the panels, while blue labels present the species identified in the shown spectra. The frequencies of the lines are shown in the upper part of each panel. The red asterisks indicate the transitions that provide the identification of *Ga-n*-C₃H₇OH. Black dotted lines indicate the $3\times\text{rms}$ level in peak intensity in the spectra. Red dotted lines show the detectability limit in integrated area defined as $3\times\text{rms}/\sqrt{N}$, with N the number of channels across the linewidth.

found for imines and acids (see García de la Concepción et al. 2021, 2022).

3.2. Search of isopropanol (*i*-propanol) and ethyl methyl ether

Isopropanol (also named isopropyl alcohol and 2-propanol) is a structural isomer of *n*-propanol. Its chemical formula is CH₃CH(OH)CH₃. We have searched for the *gauche* and *anti* conformers of *i*-propanol (*g-i*-C₃H₇OH and *a-i*-C₃H₇OH, respectively) in our dataset by using entries 060518 and 060519 of the CDMS molecular catalog (Endres et al. 2016), obtained using the spectroscopic work of Maeda et al. (2006). The *anti*

conformer is about 120 K higher in energy than the doubly-degenerate *gauche* conformer.

None of the two conformers of *i*-propanol are detected (see Table 2), with upper limits to their column densities of $\leq 8.5\times 10^{12}$ cm⁻² for *g-i*-C₃H₇OH and $\leq 3.9\times 10^{12}$ cm⁻² for *a-i*-C₃H₇OH. These column densities translate into abundance upper limits of $\leq 6.3\times 10^{-11}$ and $\leq 2.9\times 10^{-11}$ for the *gauche* and *anti* conformers of *i*-propanol, respectively.

Propanol has a third structural isomer: ethyl methyl ether (CH₃OCH₂CH₃ or methoxyethane). We have also searched for the *trans* conformer of this species (the lowest in energy) in our dataset by using the spectroscopic information reported by Fuchs et al. (2003) and by inserting the entry for this species in CDMS/JPL format into MADCUBA. This species has not

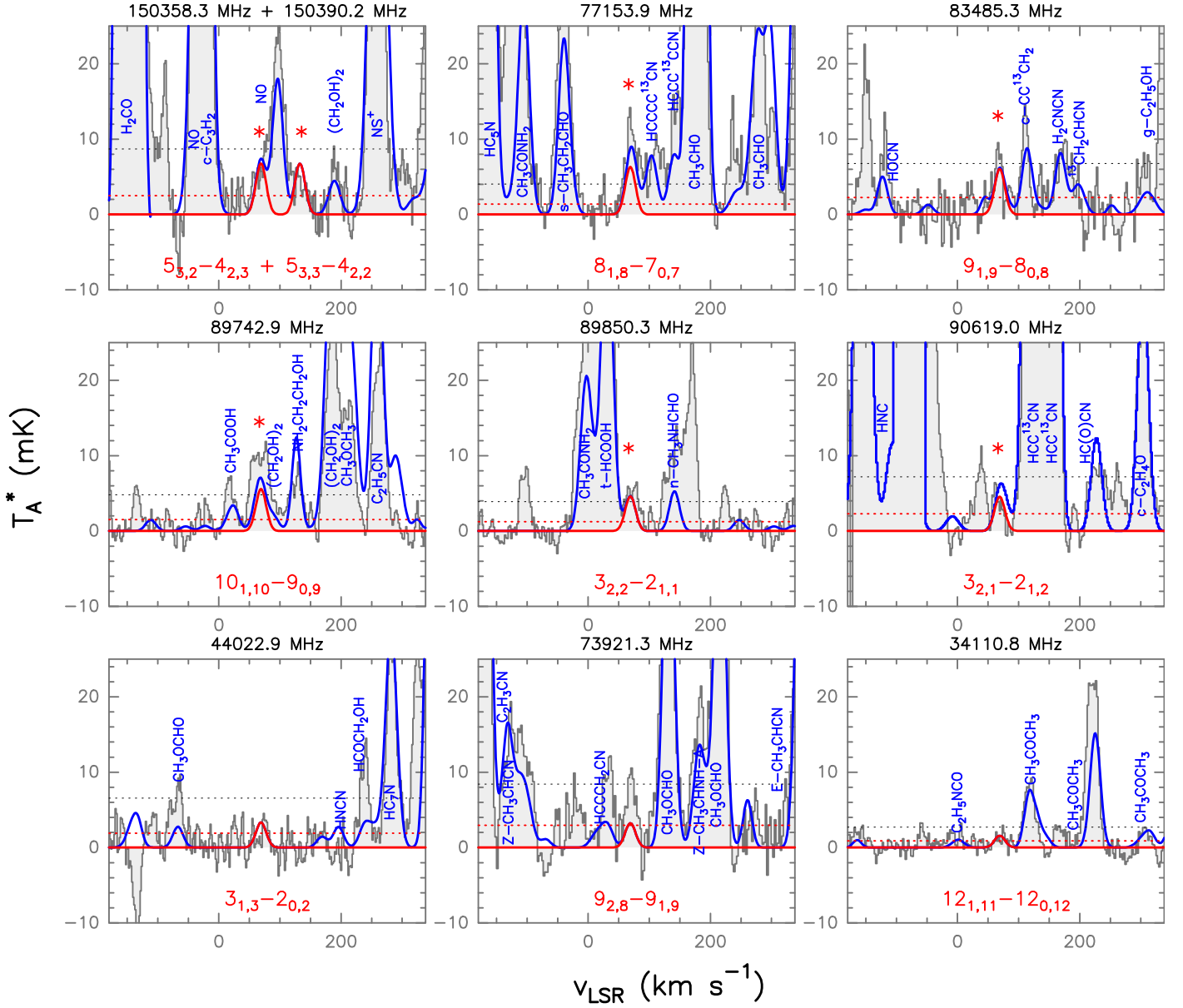


Fig. 3. Unblended and slightly blended transitions of Aa - n - C_3H_7OH detected toward G+0.693. Histogram, grey shaded area, color lines and labels are as in Figure 2. Red lines indicate the best LTE fit to the lines of Aa - n - C_3H_7OH reported in Table 1. The frequencies of the lines are shown in the upper part of each panel, while the red asterisks indicate the transitions that contribute to the identification of Aa - n - C_3H_7OH . Black dotted lines indicate the $3\times rms$ level in peak intensity in the spectra. Red dotted lines show the detectability limit in integrated area defined as $3\times rms/\sqrt{N}$, with N the number of channels across the linewidth.

Table 2. Upper limits obtained for the Gg and Gg' conformers of n -propanol, for the *anti* and *gauche* conformers of i -propanol, and for the *trans* conformer of ethyl methyl ether.

Species	Formula	Frequency (MHz)	QNs ($J''_{K_a'',K_c''} - J'_{K_a',K_c'}$)	E_u (K)	$\log I(300K)$ (nm^2 MHz)	rms (mK)	N^a (cm^{-2})	Abundance ^b
n -propanol (Gg)	Gg - n - C_3H_7OH	75699.1096	$3_{3,1} - 2_{2,1}$	75.7	-6.1471	2.3	$\leq 1.6\times 10^{13c}$	$\leq 1.2\times 10^{-10}$
		75700.5781	$3_{3,0} - 2_{2,1}$	75.7	-6.2273	2.3	-	-
n -propanol (Gg')	Gg' - n - C_3H_7OH	87730.9823	$10_{1,10} - 9_{1,9}$	97.0	-5.2641	0.9	$\leq 5.7\times 10^{12}$	$\leq 4.2\times 10^{-11}$
isopropanol (<i>gauche</i>)	g - i - C_3H_7OH	88532.3081	$4_{1,4} - 3_{1,3}$	7.5	-5.7726	1.8	$\leq 8.5\times 10^{12c}$	$\leq 6.3\times 10^{-11}$
		88538.5001	$4_{0,4} - 3_{0,3}$	7.5	-5.7737	1.8	-	-
isopropanol (<i>anti</i>)	a - i - C_3H_7OH	79734.1627	$8_{1,8} - 7_{0,7}$	137.9	-5.5140	2.7	$\leq 3.9\times 10^{12c}$	$\leq 2.9\times 10^{-11}$
		79734.1627	$8_{0,8} - 7_{1,7}$	137.9	-5.5140	2.7	-	-
ethyl methyl ether (<i>trans</i>)	t - $CH_3OCH_2CH_3$	73243.2848	$4_{2,3} - 4_{1,4}$	8.5	-5.6357	2.7	$\leq 3.8\times 10^{13}$	$\leq 2.8\times 10^{-10}$

Notes. ^(a) Upper limits to the column densities calculated assuming a $T_{ex}=12.5$ K, i.e. the same as the one derived for Aa - n - C_3H_7OH , and after fixing $V_{LSR}=69$ km s^{-1} and $\Delta v=20$ km s^{-1} (see Section 3.1). ^(b) Abundances were derived considering a H_2 column density of 1.35×10^{23} cm^{-2} (Martín et al. 2008). ^(c) Upper limits were obtained considering the two transitions shown in the Table, which appear blended in the spectra. The selected transitions are the cleanest and the brightest of all the lines covered in our observations.

been detected toward G+0.693 either, with upper limits to its column density and abundance of, respectively, $\leq 3.8 \times 10^{13} \text{ cm}^{-2}$ and $\leq 2.8 \times 10^{-10}$ (see Table 2).

3.3. Other alcohols: detection of the *syn* and *anti* forms of vinyl alcohol

We have also searched for other alcohols within our spectroscopic survey toward G+0.693. We have targeted vinyl alcohol (or ethenol, with formula $\text{H}_2\text{C}=\text{CHOH}$), cyclopropanol ($\text{c-C}_3\text{H}_5\text{OH}$) and *n*-butanol ($\text{n-C}_4\text{H}_9\text{OH}$). We have used the CDMS entries 044506 and 044507 for the *syn* and *anti* forms of vinyl alcohol ($s\text{-H}_2\text{C}=\text{CHOH}$ and $a\text{-H}_2\text{C}=\text{CHOH}$ in CDMS; Endres et al. 2016) based on the spectroscopic work of Melosso et al. (2019). The *syn* form of vinyl alcohol is the lowest in energy with the *anti* form lying about 4.6 kJ/mol (or 550 K) above the *syn* form (Rodler 1985). For cyclopropanol ($\text{c-C}_3\text{H}_5\text{OH}$), we have taken the spectroscopic information for the *gauche* conformer (the most stable one) from the work of Macdonald et al. (1978) and inserted the entry for this species in CDMS/JPL format into MADCUBA. In the same way, for *n*-butanol (both *AGa*-(E) and *AGa*-(A) methyl internal rotation substates), we have calculated their spectroscopic information from the laboratory experiments and theoretical calculations of Kawashima et al. (2021).

Of all these species, only vinyl alcohol has been detected in both *syn* and *anti* forms ($s\text{-H}_2\text{C}=\text{CHOH}$ and $a\text{-H}_2\text{C}=\text{CHOH}$, respectively) toward G+0.693. In Table 3 and Figures 4 and 5, we report the clean and slightly blended transitions of the *syn* and *anti* forms of $\text{H}_2\text{C}=\text{CHOH}$ detected toward G+0.693 with a $\text{S/N} \geq 6$ (see the transitions with asterisks). The rest of lines without asterisks are also shown in Table 3 and Figures 4 and 5, to demonstrate that they are consistent with the identification of these species and their LTE fits.

Table 3 presents 4 clean transitions and 3 slightly blended transitions of $s\text{-H}_2\text{C}=\text{CHOH}$, and 3 clean transitions and 1 slightly blended transitions of $a\text{-H}_2\text{C}=\text{CHOH}$. The $4_{2,2} \rightarrow 4_{1,3}$ and $3_{2,2} \rightarrow 3_{1,3}$ transitions of $s\text{-H}_2\text{C}=\text{CHOH}$ are blended with lines of $\text{C}_2\text{H}_5\text{CN}$ and $\text{C}_2\text{H}_3\text{CN}$ of similar intensity respectively, while the $3_{2,1} \rightarrow 3_{1,2}$ transition of $a\text{-H}_2\text{C}=\text{CHOH}$ is blended with CH_3CHO (see Table 3). The $4_{2,2} \rightarrow 4_{1,3}$ and $3_{2,1} \rightarrow 3_{1,2}$ transitions of $a\text{-H}_2\text{C}=\text{CHOH}$ also present $\text{S/N} \geq 6$. However, these ratios are overestimated and should be taken with caution since they are calculated from the LTE fit of MADCUBA-SLIM and not from the gaussian fit of the individual lines (see Table 3). As a result, these lines are not considered for the identification of $a\text{-H}_2\text{C}=\text{CHOH}$.

We have derived the physical parameters of $s\text{-H}_2\text{C}=\text{CHOH}$ and $a\text{-H}_2\text{C}=\text{CHOH}$ using the SLIM tool from MADCUBA (Martín et al. 2019). The best LTE fit for $s\text{-H}_2\text{C}=\text{CHOH}$ is obtained for a column density of $(1.11 \pm 0.08) \times 10^{14} \text{ cm}^{-2}$ and an excitation temperature of $T_{\text{ex}} = 8.0 \pm 1.0 \text{ K}$. For $a\text{-H}_2\text{C}=\text{CHOH}$, the best fit of the lines is obtained for a column density of $(1.3 \pm 0.4) \times 10^{13} \text{ cm}^{-2}$ after fixing $T_{\text{ex}} = 14 \text{ K}$ (as we did for *Ga-n*-propanol), $\Delta v = 20 \text{ km s}^{-1}$ and $V_{\text{LSR}} = 69 \text{ km s}^{-1}$. These results are consistent with those obtained through the rotational diagrams of $s\text{-H}_2\text{C}=\text{CHOH}$ and $a\text{-H}_2\text{C}=\text{CHOH}$ (see Figures A.3 and A.4 in the Appendix). Assuming a H_2 column density of $1.35 \times 10^{23} \text{ cm}^{-2}$ (Martín et al. 2008, see also Section 3.1), the derived column densities translate into molecular abundances of $(8.2 \pm 0.6) \times 10^{-10}$ for $s\text{-H}_2\text{C}=\text{CHOH}$, and of $(9.6 \pm 3.0) \times 10^{-11}$ for $a\text{-H}_2\text{C}=\text{CHOH}$. The *syn/anti* abundance ratio for $\text{H}_2\text{C}=\text{CHOH}$ is thus ~ 8.5 .

By using again Equation 3 from Rivilla et al. (2019), we find a $T_{\text{kin}} \sim 260 \text{ K}$, which is slightly higher than that measured to-

ward G+0.693 (Zeng et al. 2018). Note that if we assumed a $T_{\text{ex}} = 8.0 \text{ K}$ (i.e. the one obtained for $s\text{-H}_2\text{C}=\text{CHOH}$), the derived column density would decrease by just a factor of 1.2, which would translate into a *syn/anti* abundance ratio ~ 10 . This ratio would be consistent with a $T_{\text{kin}} \sim 240 \text{ K}$, which is still higher than that determined by Zeng et al. (2018). This may mean that the two isomers of vinyl alcohol are not in thermodynamic equilibrium.

Finally, in Table 4, we report the upper limits to the column densities and abundances obtained for cyclopropanol and *n*-butanol. The upper limits to their abundance are $\leq 1.4 \times 10^{-10}$ and $\leq 4.1 \times 10^{-11}$, respectively.

4. Discussion

4.1. Comparison of the molecular abundances of propanol and butanol with smaller alcohols

In order to gain some insight into the production efficiency of primary alcohols in the ISM, we compare the abundances and upper limits derived for *n*-propanol ($\text{n-C}_3\text{H}_7\text{OH}$) and *n*-butanol ($\text{n-C}_4\text{H}_9\text{OH}$) with those measured for methanol (CH_3OH) and ethanol ($\text{C}_2\text{H}_5\text{OH}$) toward G+0.693 (see Figure 6). The abundances of CH_3OH and $\text{C}_2\text{H}_5\text{OH}$ toward this giant molecular cloud have been provided recently by Rodríguez-Almeida et al. (2021a) and are $(1.1 \pm 0.2) \times 10^{-7}$ for CH_3OH and $(4.6 \pm 0.6) \times 10^{-9}$ for $\text{C}_2\text{H}_5\text{OH}$.

From Figure 6, it is clear that primary alcohols are produced about ten times less each time a carbon atom is added to the chain (see red squares). Indeed, $\text{C}_2\text{H}_5\text{OH}$, $\text{n-C}_3\text{H}_7\text{OH}$ and $\text{n-C}_4\text{H}_9\text{OH}$ present abundance ratios of, respectively, 0.04, 0.006, and ≤ 0.0004 with respect to CH_3OH . Note that the value above and the one shown in Figure 6 for $\text{n-C}_3\text{H}_7\text{OH}$ correspond to the sum of the abundances from both *Ga* and *Aa* conformers (see Section 3.1). The trend of decreasing abundance by roughly one order of magnitude for increasing complexity was already noted by Rodríguez-Almeida et al. (2021a) for CH_3OH and $\text{C}_2\text{H}_5\text{OH}$ as well as for thiols (with the $-\text{SH}$ group). Here, we confirm that the same trend stands when increasing the number of carbon atoms to three and four within the chemical structure of primary alcohols.

By using IRAM 30 m and ALMA data, Tercero et al. (2015) and Müller et al. (2016) reported the abundances of CH_3OH and $\text{C}_2\text{H}_5\text{OH}$ and upper limits to the abundance of *Ga-n-C}_3\text{H}_7\text{OH} and *i*-propanol toward Orion KL and SgrB2 (N2), respectively. The $\text{C}_2\text{H}_5\text{OH}/\text{CH}_3\text{OH}$ abundance ratios are ~ 0.02 for Orion KL and ~ 0.05 for SgrB2 (N2), which are consistent with that found toward G+0.693 (~ 0.04). The upper limit to the *Ga-n-C}_3\text{H}_7\text{OH}/\text{C}_2\text{H}_5\text{OH} abundance ratio determined toward SgrB2 (N2) is ≤ 0.13 , in agreement with the abundance ratio of ~ 0.14 measured toward G+0.693. For Orion KL, Tercero et al. (2015) reported a *Ga-n-C}_3\text{H}_7\text{OH}/\text{C}_2\text{H}_5\text{OH} abundance ratio of ≤ 0.017 , i.e. a factor of 10 lower than that obtained toward G+0.693. However, as noted by Müller et al. (2016), if the partition functions of $\text{C}_2\text{H}_5\text{OH}$ and *Ga-n-C}_3\text{H}_7\text{OH} are corrected from conformational and vibrational contributions, this ratio becomes ≤ 0.07 , which is of the same order of magnitude as the ones found toward SgrB2 (N2) and G+0.693.****

For *i*-propanol, the upper limit to the abundance ratio with respect to CH_3OH derived toward G+0.693 is consistent with that measured in the EMoCA survey toward the SgrB2 (N2) massive star-forming region (Müller et al. 2016). Indeed, while the *i*-propanol abundance upper limit in SgrB2 (N2) provides an *i*-propanol abundance that is ≥ 430 times lower than the abundance

Table 3. Selected lines of both forms of vinyl alcohol ($\text{H}_2\text{C}=\text{CHOH}$), *syn* (*s*) and *anti* (*a*), detected towards G+0.693.

Frequency (MHz)	QNs ($J''_{K_a, K_c} - J'_{K_a, K_c}$)	E_u (K)	$\log I(300\text{K})$ ($\text{nm}^2 \text{ MHz}$)	rms (mK)	δv (km s^{-1})	$\int T_A^* dv$ (K km s^{-1})	S/N^a	blending
<i>s</i>-$\text{H}_2\text{C}=\text{CHOH}$								
37459.19*	2 _{1,2} - 1 _{1,1}	5.09	-6.3478	1.1	2.0	0.103(0.007) ^c	14.7	clean transition ^b
39016.31*	2 _{0,2} - 1 _{0,1}	2.81	-6.1842	1.2	1.9	0.193(0.007)	25.9	clean transition ^b
40650.65*	2 _{1,1} - 1 _{1,0}	5.32	-6.2770	1.3	1.9	0.109(0.008)	13.8	clean transition ^b
74842.40*	4 _{1,4} - 3 _{1,3}	11.38	-5.3566	3.2	2.4	0.244(0.022)	10.9	slightly blended with t-HCOOH and HCCHO ^b
86557.56*	2 _{1,2} - 1 _{0,1}	5.09	-5.3840	2.4	2.1	0.454(0.016)	29.1	slightly blended with t-HCOOH and c-HCOOH ^b
142348.06*	4 _{2,2} - 4 _{1,3}	18.98	-4.7860	3.4	1.7	0.199(0.020)	10.0	blended with C ₂ H ₅ CN
151085.05*	6 _{1,6} - 5 _{0,5}	21.24	-4.5207	4.1	1.6	0.261(0.023)	11.2	slightly blended with C ₂ H ₅ CHO ^b
154490.28*	3 _{2,2} - 3 _{1,3}	15.20	-4.9105	4.3	1.6	0.227(0.024)	9.4	blended with C ₂ H ₅ CN
161794.81	5 _{2,4} - 5 _{1,5}	23.63	-4.6522	3.1	6.0	0.13(0.04)	3.1	clean transition
<i>a</i>-$\text{H}_2\text{C}=\text{CHOH}$								
72576.63	6 _{0,6} - 5 _{1,5}	19.5	-4.6023	2.0	5.0	0.096(0.021)	4.7	clean transition
77015.59*	7 _{1,6} - 7 _{0,7}	29.6	-4.2548	2.2	2.4	0.101(0.015)	6.6	slightly blended with a- ¹³ CH ₃ CH ₂ OH ^b
89757.10*	2 _{1,2} - 1 _{0,1}	5.2	-4.6954	2.1	2.0	0.167(0.013)	12.6	clean transition ^b
94064.95	9 _{1,8} - 9 _{0,9}	46.0	-4.0615	1.7	1.9	0.043(0.011)	4.0	clean transition
106949.48*	3 _{1,3} - 2 _{0,2}	7.9	-4.4184	2.7	1.7	0.224(0.016)	14.5	clean transition ^b
139916.89*	9 _{0,9} - 8 _{1,8}	41.5	-3.8023	2.1	1.7	0.074(0.012)	6.1	clean transition
152530.51	4 _{2,2} - 4 _{1,3}	19.6	-4.0754	1.9	6.4	0.162(0.022)	7.5 ^d	clean transition ^b
155160.66	3 _{2,1} - 3 _{1,2}	15.8	-4.2142	2.1	6.4	0.149(0.024)	6.3 ^d	blended with CH ₃ CHO ^b
232655.55	4 _{2,3} - 3 _{1,2}	19.5	-3.7853	4.5	8.3	0.21(0.06)	3.7	clean transition

Notes. (a) The S/N ratios are calculated from the integrated intensity of the lines inferred from the LTE fits of MADCUBA-SLIM. Note that they are not calculated from the gaussian fits of individual lines. (b) These transitions have been detected at the ≥ 3 rms noise level in peak intensity. (c) The error in the integrated intensity is calculated as $\text{rms} \times \sqrt{\delta v \times \Delta v}$, with δv the velocity resolution of the spectra and Δv the FWHM of the line emission of 20 km s^{-1} . (d) This S/N ratio should be taken with caution since the LTE fit carried out by MADCUBA-SLIM overpredicts the integrated intensity of the line. (e) Transitions that provide the identification of the species with $S/N \geq 6$ in integrated intensity.

Table 4. Derived upper limits to the column densities of other alcohols observed toward G+0.693.

Species	Formula	Frequency (MHz)	QNs ($J''_{K_a, K_c} - J'_{K_a, K_c}$)	E_u (K)	$\log I(300\text{K})$ ($\text{nm}^2 \text{ MHz}$)	rms (mK)	N^a (cm^{-2})	Abundance ^b
Cyclopropanol	c-C ₃ H ₅ OH (<i>gauche</i>)	93909.6309	3 _{3,0} - 2 _{2,1}	8.3	-5.5796	1.4	$\leq 1.8 \times 10^{13}$	$\leq 1.4 \times 10^{-10}$
n-butanol (E conf.)	AGa-(E)-n-C ₄ H ₉ OH	139389.7073	6 _{6,1} - 5 _{5,0}	22.2	-5.1710	2.2	$\leq 5.5 \times 10^{12c}$	$\leq 4.1 \times 10^{-11}$
		139389.7073	6 _{6,0} - 5 _{5,1}	22.2	-5.1710	2.2	-	-
n-butanol (A conf.)	AGa-(A)-n-C ₄ H ₉ OH	139389.7685	6 _{6,1} - 5 _{5,0}	22.2	-5.1710	2.2	$\leq 6.2 \times 10^{12c}$	$\leq 4.6 \times 10^{-11}$
		139389.7685	6 _{6,0} - 5 _{5,1}	22.2	-5.1710	2.2	-	-

Notes. (a) Upper limits to the column densities calculated assuming a $T_{ex} = 12.5 \text{ K}$, i.e. the same as the one derived for Aa-n-C₃H₇OH, and after fixing $V_{LSR} = 69 \text{ km s}^{-1}$ and $\Delta v = 20 \text{ km s}^{-1}$ (see Section 3.1). (b) Abundances were derived considering a H₂ column density of $1.35 \times 10^{23} \text{ cm}^{-2}$ (Martín et al. 2008). (c) Upper limits were obtained considering the two transitions shown in the Table, which appear blended in the spectra.

of CH₃OH, toward G+0.693 our measured upper limit gives an abundance that is ≥ 1700 times lower than that of CH₃OH (Table 2). For the rest of alcohols explored in this work, vinyl alcohol is more than two orders of magnitude less abundant than CH₃OH and a factor of 5 less abundant than C₂H₅OH, while methyl ethyl ether and cyclopropanol have abundances that are, respectively, factors of ≥ 500 and ≥ 800 lower than that of CH₃OH (see Tables 2 and 4).

Finally, if we compare the derived upper limit abundance of methyl ethyl ether (CH₃OCH₂CH₃) with the abundance of dimethyl ether (CH₃OCH₃) found toward G+0.693 (of 8.2×10^{-9} ; Requena-Torres et al. 2006), we find that dimethyl ether is a factor ≥ 30 more abundant than methyl ethyl ether, which is also consistent with the idea that the abundance of these COMs decreases by roughly one order of magnitude with the addition of a -CH₂ group to their molecular structure.

4.2. Chemistry of propanol and butanol in G+0.693

The chemistry of large alcohols was theoretically studied by Charnley et al. (1995) for the case of a massive hot molecular core. In this work, species such as CH₃OH, C₂H₅OH, propanol

(both n-C₃H₇OH and *i*-C₃H₇OH) and butanol (n-C₄H₉OH and *t*-C₄H₉OH) were assumed to be formed on the surface of dust grains and injected into the gas phase by the thermal evaporation of the grain mantles. The subsequent gas-phase chemistry yields pure ethers through, mainly, alkyl transfer and proton transfer reactions. Charnley et al. (1995) considered that the initial ice mantle abundance of propanol and butanol were, respectively, factors of 10 and 100 lower than that of solid ethanol.

In Section 4.1, we reported a similar trend for these large alcohols to decrease their abundance in G+0.693 by approximately a factor of 10 with the addition of a carbon atom. If we thus compare the modelling results of Charnley et al. (1995) with our measured abundances, the best match is found for the case with initial ice mantle abundances of 10^{-6} , 10^{-7} and 10^{-8} for C₂H₅OH, propanol and butanol, respectively. Indeed, at time-scales of 10^5 yrs (the typical time-scales that explain the rich chemistry in complex organics toward Galactic Center giant molecular clouds; see Requena-Torres et al. 2006), the predicted abundance of C₂H₅OH, propanol and butanol in the gas phase are, respectively, $\sim 4 \times 10^{-9}$, $\sim 2 \times 10^{-10}$, and $\sim 1.5 \times 10^{-11}$ (see Figure 3 in Charnley et al. 1995). These values are strikingly similar to those measured in G+0.693, i.e. $(4.6 \pm 0.6) \times 10^{-9}$ for

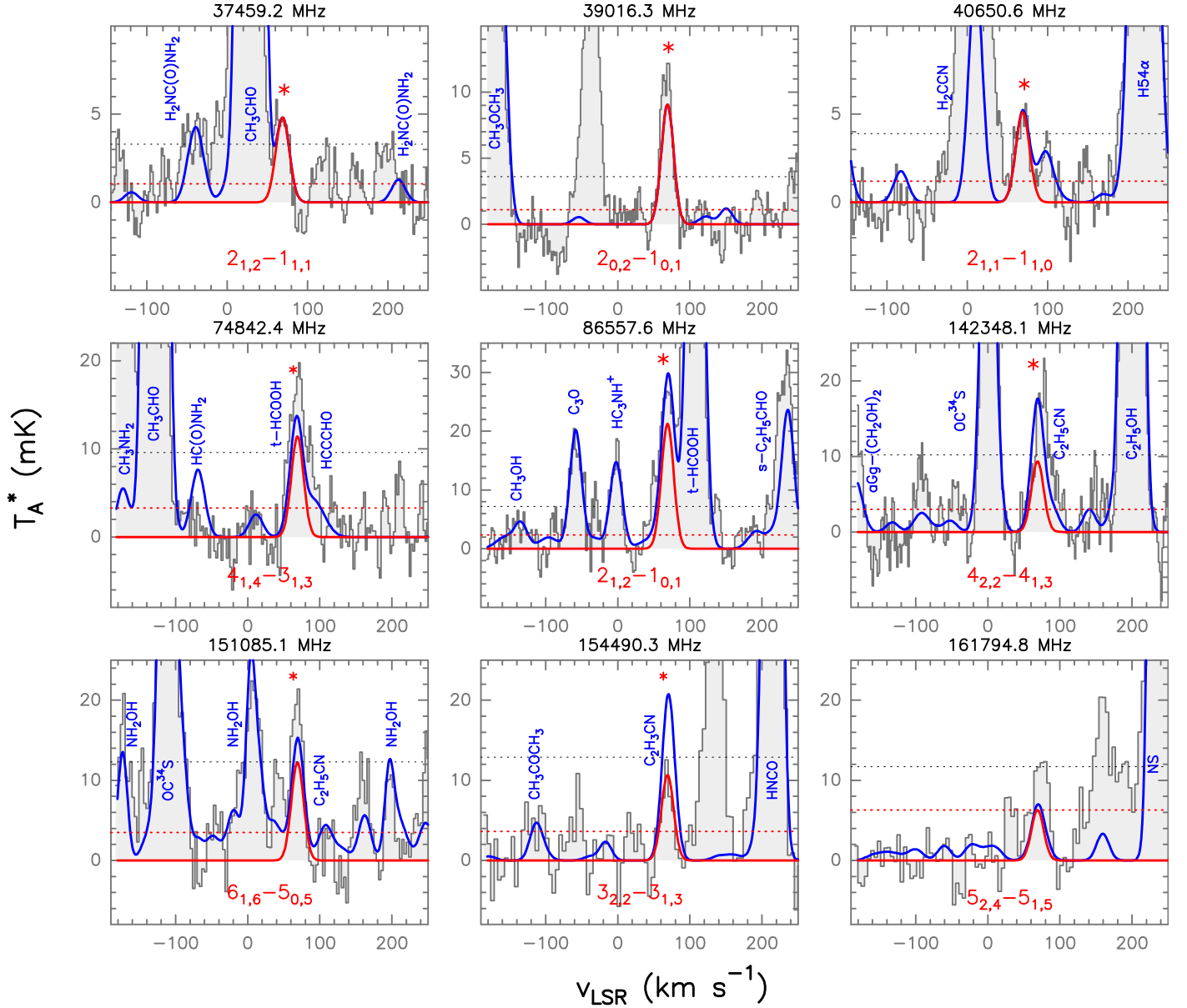


Fig. 4. Unblended and slightly blended transitions of s -H₂C=CHOH detected toward G+0.693. For a description of the colours displayed in the plot, see Figure 2. The spectroscopic information and the derived parameters from the best LTE fit of these lines, are reported in Table 3. The frequencies of the lines are shown in the upper part of each panel, while the red asterisks indicate the transitions that contribute to the identification of s -H₂C=CHOH. Black dotted lines indicate the $3\times\text{rms}$ level in peak intensity in the spectra. Red dotted lines show the detectability limit in integrated area defined as $3\times\text{rms}/\sqrt{N}$, with N the number of channels across the linewidth.

C₂H₅OH (Rodríguez-Almeida et al. 2021a), $(6.6\pm 0.5)\times 10^{-10}$ for propanol, and $\leq 4\times 10^{-11}$ for butanol (see blue triangles in Figure 6). This suggests that, even after gas-phase chemistry takes over, the decrease in the abundance of CH₃OH, C₂H₅OH, propanol and butanol by roughly one order of magnitude with an increasing number of carbon atoms is preserved in the gas phase, which may allow us to indirectly constrain the amount formed in the ices for these alcohols.

We note, however, that while the modelled propanol/C₂H₅OH abundance ratio is 0.05 (see Figure 3 in Charnley et al. 1995), the same ratio measured in G+0.693 gives 0.15, which suggests that propanol is more efficiently produced under the highly energetic processing of the ISM in the Galactic Center than in typical Galactic hot cores (see Section 4.1 above). In addition, as pointed out by Requena-Torres et al. (2006), the models of Charnley et al. (1995) cannot explain

the homogeneity of the COMs abundances across the different GMCs in the Central Molecular Zone. Instead, a continuous replenishment of complex organic material from dust grains into the gas phase by large-scale shocks in the highly turbulent ISM of the Galactic Center, needs to be invoked.

In the work of Charnley et al. (1995), it is assumed that propanol and butanol are present in ices, but it is not explained how these species are formed. In the more recent chemical models of Manigand et al. (2021), propanol is formed on the surface of dust grains via two routes: 1) the successive hydrogenation of C₃O; and 2) the radical-radical reaction between O and C₃H₈. The latter has two possible outcomes, $\text{O} + \text{C}_3\text{H}_8 \rightarrow \text{C}_3\text{H}_7\text{OH}$ and $\text{O} + \text{C}_3\text{H}_8 \rightarrow \text{H}_2\text{O} + \text{C}_3\text{H}_6$, with branching ratios of 20% and 80%, respectively. The models are applied to the case of the IRAS16293-2422 B low-mass hot corino, for which upper limits to the abundance of propanol have been derived (Qasim et

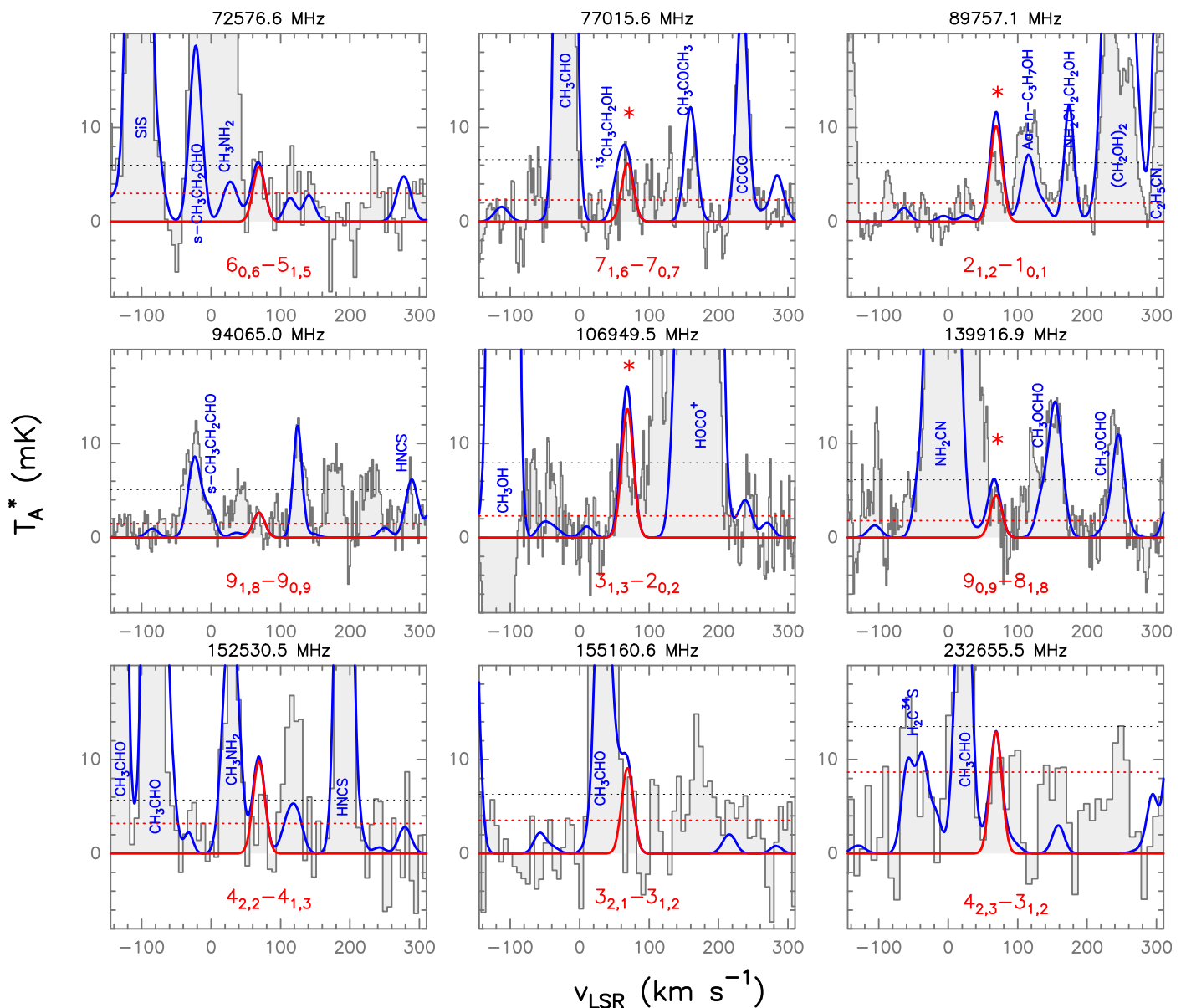


Fig. 5. Unblended and slightly blended transitions of α -H₂C=CHOH detected toward G+0.693. For a description of the colours displayed in the plot, see Figure 2. The spectroscopic information and the derived parameters from the best LTE fit of these lines, are reported in Table 3. The frequencies of the lines are shown in the upper part of each panel. Red asterisks indicate the transitions that contribute to the identification of α -H₂C=CHOH. Black dotted lines indicate the $3\times$ rms level in peak intensity in the spectra. Red dotted lines show the detectability limit in integrated area defined as $3\times$ rms/ \sqrt{N} , with N the number of channels across the linewidth.

al. 2019; Manigand et al. 2021). The results of Manigand et al. (2021) only reproduce the factor of 10 difference between the abundances of propanol and C₂H₅OH in the gas phase at the end of the simulations for models A1-E1, where an efficient destruction of C₃ through the gas-phase reaction $O + C_3 \rightarrow C_2 + CO$ is considered (see Table D1 in this work). We note, however, that the absolute abundances of propanol and C₂H₅OH predicted by these models clearly exceed the values observed toward G+0.693 (of $\geq 10^{-7}$ - 10^{-6} ; Manigand et al. 2021).

Laboratory experiments carried out by Qasim et al. (2019) explored alternative formation routes for the formation of propanol in the ices such as the in-situ recombination of HCO (formed after the hydrogenation of CO) with radicals formed via the processing of C₂H₂. This yields n -propanol after several hydrogenation steps where propenal (CH₂CHCHO) and propanal (CH₃CH₂CHO) are intermediate steps. These species have been

detected toward G+0.693 with abundances of 2.7×10^{-10} for CH₂CHCHO and of 1.2×10^{-9} for CH₃CH₂CHO (see Table 4 in Requena-Torres et al. 2008)³. The abundance of CH₃CH₂CHO is a factor of ~ 2 higher than that of n -propanol, which is consistent with the idea that all these species form concurrently on the surface of dust grains. The non-diffusive mechanism proposed by Qasim et al. (2019) likely dominates the formation of these species toward G+0.693 since the dust grain temperatures in this source lie below 25 K (Rodríguez-Fernández et al. 2000).

³ Note that the abundances shown in Table 4 of Requena-Torres et al. (2008) were obtained assuming a H₂ column density of 4.1×10^{22} cm⁻². Therefore, these abundances have been corrected by the H₂ column density assumed in this work of 1.35×10^{23} cm⁻² inferred from C¹⁸O data by Martín et al. (2008).

4.3. Vinyl alcohol: comparison with previous observations

Vinyl alcohol has been reported tentatively in the past toward the massive hot molecular core SgrB2(N) (Turner & Aponi 2001). More recently and thanks to a high-sensitivity spectroscopic survey carried out toward the molecular dark cloud TMC-1 with the Yebes 40m telescope, the *syn* conformer of vinyl alcohol ($s\text{-H}_2\text{C=CHOH}$) was unambiguously identified (Agúndez et al. 2021). Our observations toward G+0.693 not only confirm the presence of $s\text{-H}_2\text{C=CHOH}$ in the ISM, but also present the first robust detection of the *anti* conformer of vinyl alcohol ($a\text{-H}_2\text{C=CHOH}$) in space (see Section 3.3).

Vinyl alcohol is a structural isomer of acetaldehyde (CH_3CHO) and therefore previous works have compared the abundance of both chemical species. Turner & Aponi (2001) showed that the column density of vinyl alcohol derived toward SgrB2(N) is similar to that measured for acetaldehyde. This is consistent with the results of Agúndez et al. (2021) toward TMC-1, where the abundance ratio $s\text{-H}_2\text{C=CHOH/CH}_3\text{CHO}$ is ~ 1 . In contrast, Martin-Drumel et al. (2019) did not detect vinyl alcohol in the EMOCA survey toward the high-mass star-forming region SgrB2(N2) (Belloche et al. 2016), with an abundance ratio $s\text{-H}_2\text{C=CHOH/CH}_3\text{CHO} \leq 0.08$.

Toward G+0.693, the measured abundance of CH_3CHO is 3.7×10^{-9} (Sanz-Novo et al. 2022), while the total abundance of vinyl alcohol (considering both the *syn* and *anti* forms) is $\sim 9 \times 10^{-10}$. This implies that vinyl alcohol is a factor of ~ 4 less abundant than CH_3CHO toward the G+0.693 Galactic Center molecular cloud, with a $\text{H}_2\text{C=CHOH/CH}_3\text{CHO}$ abundance ratio of 0.25 ± 0.02 . This value lies between the abundance ratios found toward TMC-1 (of 1.0 ± 0.2 ; Agúndez et al. 2021) and SgrB2(N) (of ~ 1 , although this value has large uncertainties; see Turner & Aponi 2001), and the one measured toward SgrB2(N2) (of ≤ 0.08 ; Martin-Drumel et al. 2019). The lack of detection of vinyl alcohol toward the SgrB2(N2) compact hot cores is consistent with the idea that the emission of vinyl alcohol arises mainly from the envelope of the SgrB2 molecular cloud. In Section 4.4, we discuss the possible chemical routes for the formation of vinyl alcohol.

4.4. Chemistry of vinyl alcohol in G+0.693

For vinyl alcohol, both gas-phase and grain-surface formation reactions have been proposed. For gas-phase formation, Agúndez et al. (2021) concluded that the most likely mechanism for the formation of this species is the dissociative recombination of CH_3CHOH^+ , for which the CCO backbone is formed with a branching ratio of 23% (Hamberg et al. 2010). The subsequent hydrogenation of CCO could form vinyl alcohol together with acetaldehyde (Agúndez et al. 2021), although the branching ratios are unknown. We also note that the gas-phase reactions $\text{OH} + \text{C}_2\text{H}_4$ and $\text{OH} + \text{CH}_2\text{CHCH}_3$ could also yield vinyl alcohol, although they present activation barriers (Zhu et al. 2005; Zádor et al. 2009).

For grain-surface reactions, vinyl alcohol has been generated in interstellar ice analogues under proton irradiation of $\text{H}_2\text{O/C}_2\text{H}_2$ ices (Hudson & Moore 2003) or electron irradiation of CO/CH_4 and $\text{H}_2\text{O/CH}_4$ ices (Abplanalp et al. 2015; Bergantini et al. 2017). More recent experiments of non-energetic processing of ices also show that the co-deposition of C_2H_2 together with O_2 and H atoms induces the formation of vinyl alcohol and acetaldehyde under low temperature conditions ($T=10\text{K}$; see Chuang et al. 2020). Unfortunately, these works do not provide information about the branching ratios for the two species, and

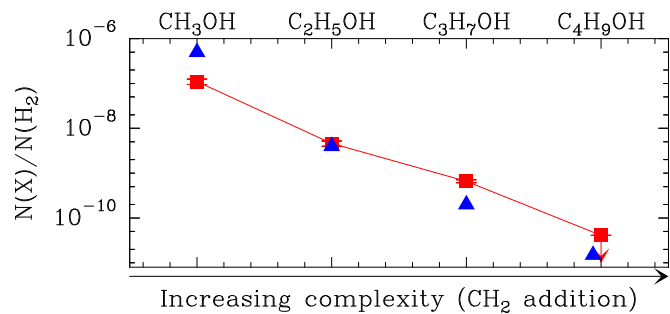


Fig. 6. Comparison of the molecular abundances of the primary alcohols methanol, ethanol, *n*-propanol and *n*-butanol measured toward the giant molecular cloud G+0.693 (red squares) with the values predicted by the models of Charnley et al. (1995, blue triangles) for the case with initial solid abundances of 10^{-6} , 10^{-7} and 10^{-8} for $\text{C}_2\text{H}_5\text{OH}$, propanol and butanol, respectively. Error bars are shown also in red for the measured abundances, and the downward red arrow indicates an upper limit.

therefore, it is not possible to assess which mechanism dominates the production of vinyl alcohol.

For the case of the Galactic Center molecular cloud G+0.693, multiple routes (both gas-phase and grain-surface) may indeed be at play since its chemistry is dominated by shocks and high cosmic-ray ionization rates (see e.g. Zeng et al. 2018). The kinetic temperatures of the molecular gas toward this source (of 70-150 K; Zeng et al. 2018) could help overcome the activation barriers of the reactions $\text{OH} + \text{C}_2\text{H}_4$ and $\text{OH} + \text{CH}_2\text{CHCH}_3$ (see above; Zhu et al. 2005; Zádor et al. 2009). In addition, although the temperature of dust is low toward this cloud, the high radiation field of secondary UV photons (induced by the high cosmic-rays ionization rate measured in the Galactic Center, which is factors 100-1000 higher than the standard value; see Goto et al. 2014) could process the ices, generating enough radicals that could react *in-situ* on the surface forming vinyl alcohol. A detailed chemical modelling of the G+0.693 source is needed to assess all these different formation mechanisms.

We finally note that the isomerization transformation of acetaldehyde into vinyl alcohol is not possible (either in the gas phase or in water ices) due to the large relative energies between both species and to the large activation energy barriers involved in this transformation (see Perrero et al. 2022).

4.5. Alcohols as precursors of lipids in primitive Earth

Understanding the emergence of membranes is central to the problem of the origin of life. Membranes are indeed a key element since they enable the encapsulation and protection of the genetic information required for replication and of nutrients needed for metabolic processes (Ruiz-Mirazo et al. 2014). Current cell membranes are formed by a bilayer of phospholipids, i.e. amphiphilic molecules that contain a polar head and a non-polar, hydrophobic tail. Phospholipids, however, present a rather complex structure with an alcohol phosphate group (the polar hydrophilic head, where ethanolamine is one of the possible head groups; Rivilla et al. 2021a), a glycerol, and two hydrocarbon chains derived from fatty acids (the nonpolar hydrophobic tails). Because of this complexity, it is believed that these structures likely appeared biosynthetically at a later stage as a result of the cell's own machinery (see Ruiz-Mirazo et al. 2014, and references therein).

Alternatively, simpler amphiphilic molecules have been proposed as prebiotic lipids such as fatty alcohols or even prenols, i.e. single-chain unsaturated alcohols that present double bonds

(Ourisson et al. 1995). These amphiphilic compounds can assemble bi-layered supramolecular aggregates such as vesicles when they come in contact with water thanks to the so-called *hydrophobic effect*⁴ and to van der Waals interactions. The discovery in the ISM of *n*-propanol (a small chain primary alcohol) and of vinyl alcohol (a small alcohol with a double bond; see Sections 3.1 and 3.3) thus opens the possibility that these molecules were sourced into a primitive Earth through the impact of meteorites and comets, possibly representing precursors of prebiotic lipids such as fatty alcohols and prenols. The fact that alcohols up to pentanol not only have been detected in comets such as 67P/Churyumov-Gerasimenko (Altwegg et al. 2019) but also in carbonaceous chondrites such as the Murray and Orgueil meteorites (Jungclauss et al. 1976; Sephton 2002), support the hypothesis of an exogenous delivery of precursors of prebiotic lipids into an early Earth.

5. Conclusions

In this paper we report the discovery of *n*-propanol in the ISM with the detection of the two lowest-energy conformers, *Ga*-*n*-C₃H₇OH and *Aa*-*n*-C₃H₇OH. *n*-propanol was detected toward the GMC G+0.693 located in the Galactic Center and known to be one of the richest repository of complex organic molecules in our Galaxy. The derived abundance of *n*-propanol (considering both *Ga* and *Aa* conformers) is 6.6×10^{-10} . By comparing this abundance with those of methanol and ethanol measured toward the same source, we find that the abundance of primary alcohols drops by approximately a factor of 10 by increasing complexity (i.e. by inserting a new CH₂ group).

Finally, we also report the detection of both *syn* and *anti* conformers of vinyl alcohol (H₂C=CHOH) toward G+0.693. To our knowledge, this is the first time the latter conformer (*anti*) is firmly detected in the ISM. The derived abundance ratio between vinyl alcohol and acetaldehyde (its structural isomer) toward G+0.693 (of ~0.25), lies between the ones found toward TMC-1 and the SgrB2(N) molecular envelope (Turner & Aponi 2001; Agúndez et al. 2021), and the upper limit measured toward the SgrB2(N2) compact hot core (Martín-Drumel et al. 2019). The detection of these alcohols toward G+0.693 opens the possibility for precursors of prebiotic lipids to form in the ISM.

Acknowledgements. We would like to thank Carlos Briones for the fruitful discussions on possible prebiotic precursors of phospholipids and the formation of the first cell membranes. We also acknowledge the constructive and detailed report from an anonymous referee, who helped to improve the original version of the manuscript. Based on observations carried out with the IRAM 30m and Yebes 40m telescopes through projects 172-18 (PI: J. Martín-Pintado), 018-19 (PI: V. M. Rivilla) and 20A008 (PI: I. Jiménez-Serra). IRAM is supported by INSU/CNRS (France), MPG (Germany) and IGN (Spain). The 40m radiotelescope at Yebes Observatory is operated by the Spanish Geographic Institute (IGN, Ministerio de Transportes, Movilidad y Agenda Urbana). I.J.-S. and J.M.-P. have received partial support from the Spanish State Research Agency (AEI) through project numbers PID2019-105552RB-C41 and MDM-2017-0737 Unidad de Excelencia "María de Maeztu" - Centro de Astrobiología (CSIC/INTA). L.F.R.-A. acknowledges support from a JAE-intro ICU studentship funded by the Spanish National Research Council (CSIC). L.F.R.-A., V.M.R. and L.C. also acknowledge support from the Comunidad de Madrid through the Atracción de Talento Investigador Modalidad I (Doctores con experiencia) Grant (COOL: Cosmic Origins of Life; 2019-T1/TIC15379; PI: V.M.Rivilla). P.d.V. and B.T. thank the support from the European Research Council through Synergy Grant ERC-2013-SyG, G.A. 610256 (NANOCOSMOS) and from the Spanish Ministerio de Ciencia e Innovación (MICIU) through project PID2019-107115GB-C21. B.T. also acknowledges the Spanish MICIU for funding support from grant PID2019-106235GB-I00.

⁴ The hydrophobic effect is the observed trend for nonpolar substances to aggregate and exclude water molecules in an aqueous solution.

References

- Abplanalp, M. J., Borsuk, A., Jones, B. M., & Kaiser, R. I. 2015, *ApJ*, 814, 45
 Agúndez, M., Marcelino, N., Tercero, B., Cabezas, C., de Vicente, P., & Cernicharo, J. 2021, *A&A*, 649L, 4A
 Altwegg, K., Balsiger, H., & Fuselier, S. A. 2019, *ARA&A*, 57, 113A
 Bakri, B., Demaison, J., Margulés, L., & Møllendal, H. 2001, *J. Mol. Spectrosc.*, 208, 92
 Bar-On, Y. M., Phillips, R., & Milo, R. 2018, *PNAS*, 115 (25), 6506-6511
 Becker, S., Feldmann, J., Wiedemann, S., et al. 2019, *Science*, 366, 76B
 Belloche, A., Müller, H. S. P., Garrod, R. T., & Menten, K. M. 2016, *A&A*, 587, A91
 Belloche, A., Garrod, R. T., Müller, H. S. P., et al. 2019, *A&A*, 628A, 10B
 Bergantini, A., Maksyutenko, P., & Kaiser, R. I. 2017, *ApJ*, 841, 96
 Bernstein, M. P., Sandford, S. A., Allamandola, L. J., Gillette, J. S., Clemett, S. J., & Zare, R. N. 1999, *Science*, 283, 1135
 Blom, C. E., & Bauder A. 1981, *Chem. Phys. Lett.*, 82, 492.
 Charnley, S. B., Kress, M. E., Tielens, A. G. G. M., & Millar, T. J. 1995, *ApJ*, 448, 232C
 Chuang, K.-J., Fedoseev, G., Qasim, D., et al. 2020, *A&A*, 635, A199
 Chyba, C., & Sagan, C. 1992, *Nature*, 355, 125.
 Davis, R. W., & Gerry, M. C. L. 1976, *Journal of Mol. Spec.*, 59, 407
 Deamer, D. W. 1985, *Nature*, 317, 792
 Deamer, D. W., Mahon, E. H., & Bosco, G. 1994, In *Early Life on Earth*, Nobel Symposium; Bengtson, S., Ed. Columbia University Press: New York, Vol. 84.
 Dreizler, H., & Scappini, F., 1981, *Zeitschrift für Naturforschung A.*, 36, 11, 1187
 Endres C.P., Schlemmer S., Schilke P., et al. 2016, *J. Mol. Spectrosc.*, 327, 95
 Fuchs, U., Winnewisser, G., Groner, P., De Lucia, Frank C., & Herbst, E. 2003, *ApJS*, 144, 277F
 Garay, G., & Lizano, S. 1999, *PASP*, 111, 1049G
 García de la Concepción, J., Jiménez-Serra, I., Carlos Corchado, J., Rivilla, V. M., & Martín-Pintado, J. 2021, *ApJ*, 912L, 6G
 García de la Concepción, J., Colzi, L., Jiménez-Serra, I., Molpeceres, G., Corchado, J. C., et al. 2022, *A&A*, 658A, 150G
 Goto, M., Geballe, T. R., Indriolo, Nick., et al. 2014, *ApJ*, 786, 96G
 Hamberg, M., Zhaunerchyk, V., Vigren, E., et al. 2010, *A&A*, 522, A90
 Hudson, R. L., & Moore, M. H. 2003, *ApJ*, 586, L107
 Ilyushin, V. V., Endres, C. P., Lewen, F., Schlemmer, S. & Drouin, B. J. 2013, *J. Mol. Spectrosc.*, 290, 31
 Jaman, A. I., Chakraborty, S., & Chakraborty, R. 2015, *Journal of Molecular Structure*, 1079, 402
 Jiménez-Serra, I., Martín-Pintado, J., Rivilla, V. M. et al. 2020, *AsBio*, 20, 1048J
 Jiménez-Serra, I., Caselli, P., Martín-Pintado, J., & Hartquist, T. W. 2008, *A&A*, 482, 549J
 Jørgensen, J. K., Belloche, A., Garrod, R. T. 2020, *ARA&A*, 58, 727J
 Jungclauss, G. A., Yuen, G. U., Moore, C.B., & Lawless, J.G. 1976, *Meteoritics*, 11, 231
 Kawashima, Y., Tanaka, Y., Uzuyama, T., & Hirota, E. 2021, *J. Phys. Chem. A*, 125, 1166
 Kisiel, Z., et al. 2010 *Phys. Chem. Chem. Phys.*, 12, 8329
 Macdonald, J. N., Norbury, D., & Sheridan, J. 1978, *J. Chem. Soc., Faraday Trans. 2*, 74, 1365
 Maeda, A., Medvedev, I. R., De Lucia, F. C., Herbst, E. 2006, *ApJS*, 166, 650M
 Manigand, S., Coutens, A., Loison, J. -C., Wakelam, V., Calcutt, H., et al. 2021, *A&A*, 645A, 53M
 Margulés, L., Ilyushin, V. V., McGuire, B. A., Belloche, A., Motiyenko, R. A., et al. 2020, *J. Mol. Spectrosc.*, 371, 111304
 Marstokk, K. M. & Møllendal, H. 1973, *J. Mol. Struct.*, 15, 137
 Martín, S., Requena-Torres M.A., Martín-Pintado, J., et al. 2008, *ApJ*, 678, 245
 Martín, S., Martín-Pintado, J., Blanco-Sánchez, C., Rivilla, V. M., Rodríguez-Franco, A., & Rico-Villas, F. 2019, *A&A*, 631A, 159M
 Martín, S., et al. 2021, *A&A*, in press, arXiv:2109.08638
 Martín-Drumel, M.-A., Lee, K. L. K., Belloche, A., Zingsheim, O., Thorwirth, S., et al. 2019, *A&A*, 623A, 167M
 McCollom, T. M., Ritter, G., & Simoneit, B. R. T. 1999, *Origins Life Evol. Biospheres*, 29, 153
 Melosso, M., McGuire, B. A., Tamassia, F., Degli Esposti, C., & Dore, L. 2019, *ACS Earth and Space Chemistry*, 3, 1189M
 Müller, H. S. P., Belloche, A., Xu, L.-H., Lees, R. M., Garrod, R. T., et al. 2016, *A&A*, 587A, 92M
 Nooner, D. W., Gibert, J. M., Gelpi, E., & Oró, J. 1976, *Geochim. Cosmochim. Acta*, 40, 915.
 Ourisson, G., & Nakatani, 1995, *Y. Chem. Biol.*, 2, 631
 Perrero, J., Enrique-Romero, J., Martínez Bachs, B., Ceccarelli, C., Balucani, N., et al. 2022, *ACS Earth and Space Chemistry*, in press, arXiv:2202.11406
 Pszczółkowski, L., Białkowska-Jaworska, E., & Kisiel Z. 2005, *Journal of Mol. Spec.*, 234, 106

- Qasim, D., Fedoseev, G., Chuang, K. -J., Taquet, V., Lamberts, T., et al. 2019, *A&A*, 627A, 1Q
- Requena-Torres M.A., Martín-Pintado J., Rodríguez-Fernández N.J., et al. 2006, *A&A*, 455, 971
- Requena-Torres M.A., Martín-Pintado J., Martín S. et al., 2008, *ApJ*, 672, 352
- Rivilla V.M., Martín-Pintado J., Jiménez-Serra I., et al. 2019, *MNRAS*, 483, L114
- Rivilla V.M., Martín-Pintado J., Jiménez-Serra I., et al. 2020, *ApJL*, 899, L28
- Rivilla, V. M., Jiménez-Serra, I., Martín-Pintado, J., et al. 2021, *PNAS*, 11801314R
- Rivilla, V. M., Jiménez-Serra, I., García de la Concepción, J., et al. 2021, *MNRAS*, 506L, 79R
- Rivilla, V. M., García de la Concepción, J., Jiménez-Serra, I., Martín-Pintado, J., Colzi, L., et al. 2022, *Frontiers in Astronomy and Space Sciences*, in press, arXiv:2202.13928
- Rodler, 1985, *J. Mol. Spectrosc.*, 114, 23
- Rodríguez-Almeida, L., Jiménez-Serra, I., V. M. Rivilla et al. 2021, *ApJ*, 912L, 11R
- Rodríguez-Almeida, L., et al. 2021, *A&A*, 654L, 1R
- Rodríguez-Fernández, N. J., Martín-Pintado, J., de Vicente, P., Fuente, A., Hüttemeister, S., Wilson, T. L., & Kunze, D. 2000, *A&A*, 356, 695R
- Ruiz-Mirazo, K., Briones, C., & de la Escosura, A., 2014, *Chem. Rev.*, 114, 285
- Sanz-Novo, M., Belloche, A., Rivilla, V. M., Garrod, R. T., Alonso, J. L. et al. 2022, *A&A*, in press, arXiv:2203.07334
- Sephton, M. A. 2002, *Nat. Prod. Rep.*, 19, 292
- Tercero F, López-Pérez J.A., Gallego J.D., et al. 2021, *A&A*, 645, 22
- Tercero, B., Cernicharo, J., López, A., et al. 2015, *A&A*, 582L, 1T
- Turner, B. E., & Apponi, A. J. 2001, *ApJ*, 561L, 207T
- Zádor, J., Jasper, A. W., & Miller J. A. 2009, *Phys. Chem. Chem. Phys.*, 11, 11040
- Zeng S., Jiménez-Serra I., Rivilla, V.M., et al. 2018, *MNRAS*, 478, 2962
- Zeng S., Zhang Q., Jiménez-Serra I., et al. 2020, *MNRAS*, 497, 4896
- Zhu, R. S., Park, J., & Lin, M. C. 2005, *Chem. Phys. Lett.*, 408, 25

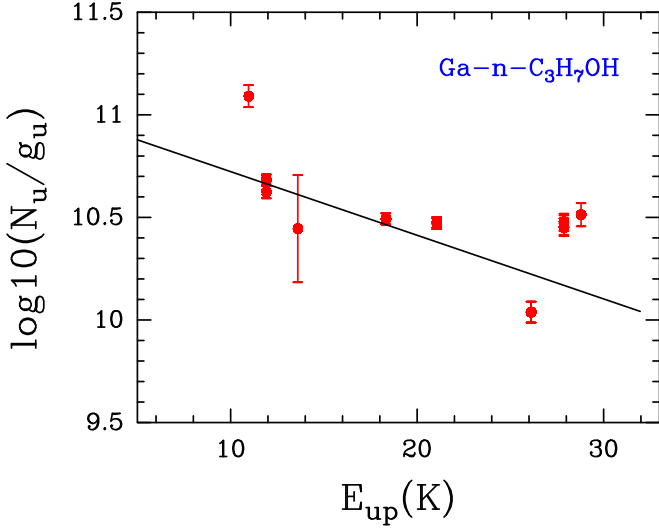


Fig. A.1. Rotational diagram obtained by using the rotational transitions of *Ga-n-C₃H₇OH* reported in Table 1. The derived parameters are $T_{ex}=16.9\pm 3.1$ K and $N=6.6\pm 2.3\times 10^{13}$ cm⁻².

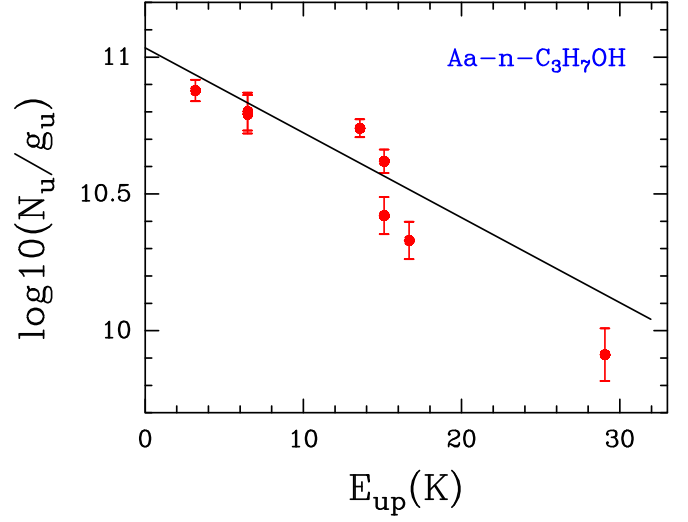


Fig. A.2. Rotational diagram obtained by using the rotational transitions of *Aa-n-C₃H₇OH* reported in Table 1, except the $9_{2,8}\rightarrow 9_{1,9}$ and $10_{1,10}\rightarrow 9_{0,9}$ lines that are blended with U species. The derived parameters are $T_{ex}=14.0\pm 3.4$ K and $N=5.1\pm 2.2\times 10^{13}$ cm⁻².

Appendix A: Rotational Diagrams

In this Section, we show the rotational diagrams obtained for *Ga-n-C₃H₇OH*, *Aa-n-C₃H₇OH*, *s-H₂C=CHOH* and *a-H₂C=CHOH* (see Figures A.1, A.2, A.3, and A.4), which have been detected toward G+0.693. The goal is to establish the reliability of the excitation temperatures (T_{ex}) and column densities (N) derived by Madcuba (see Sections 3.1 and 3.3). For these diagrams, we have used all molecular transitions reported in Tables 1 and 3, except for *Aa-n-C₃H₇OH* for which we have not considered the $9_{2,8}\rightarrow 9_{1,9}$ and $10_{1,10}\rightarrow 9_{0,9}$ transitions that appear blended with U species.

The results of the rotational diagrams are: $T_{ex}=16.9\pm 3.1$ K and $N=6.6\pm 2.3\times 10^{13}$ cm⁻² for *Ga-n-C₃H₇OH*; $T_{ex}=14.0\pm 3.4$ K and $N=5.1\pm 2.2\times 10^{13}$ cm⁻² for *Aa-n-C₃H₇OH*; $T_{ex}=8.715\pm 0.008$ K and $N=1.5\pm 0.3\times 10^{14}$ cm⁻² for *s-H₂C=CHOH*; and $T_{ex}=17.0\pm 2.4$ K and $N=1.5\pm 0.4\times 10^{13}$ cm⁻² for *a-H₂C=CHOH*. These values are consistent with those obtained by Madcuba.

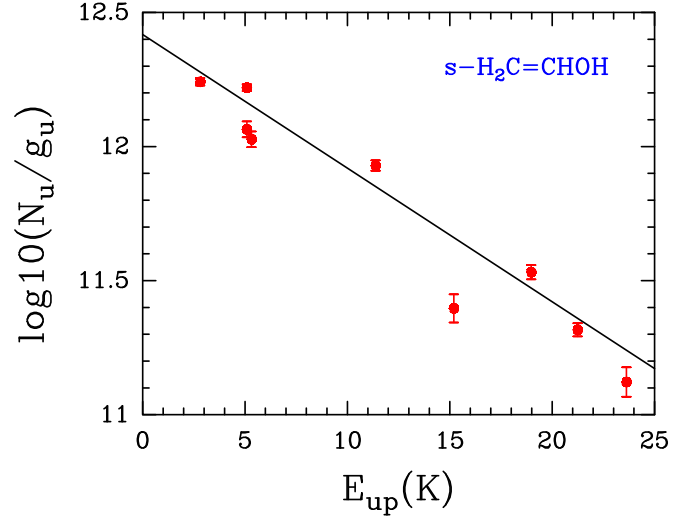


Fig. A.3. Rotational diagram obtained by using the rotational transitions of *s-H₂C=CHOH* reported in Table 3. The derived parameters are $T_{ex}=8.715\pm 0.008$ K and $N=1.5\pm 0.3\times 10^{14}$ cm⁻².

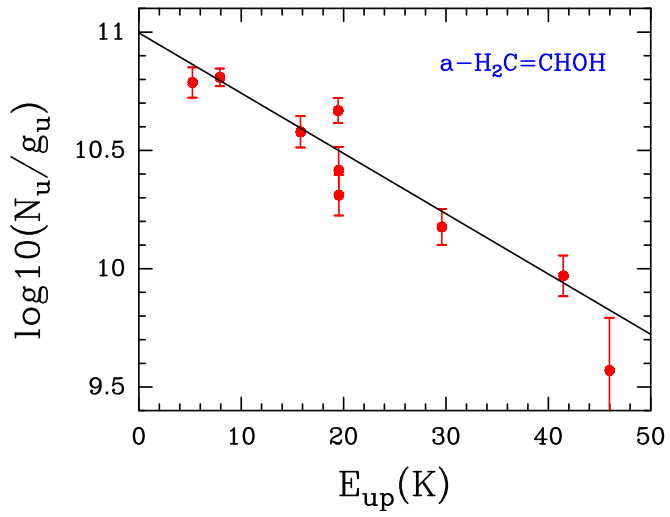


Fig. A.4. Rotational diagram obtained by using the rotational transitions of $\alpha\text{-H}_2\text{C=CHOH}$ reported in Table 3. The derived parameters are $T_{ex}=17.0\pm 2.4$ K and $N=1.5\pm 0.4\times 10^{13}$ cm^{-2} .